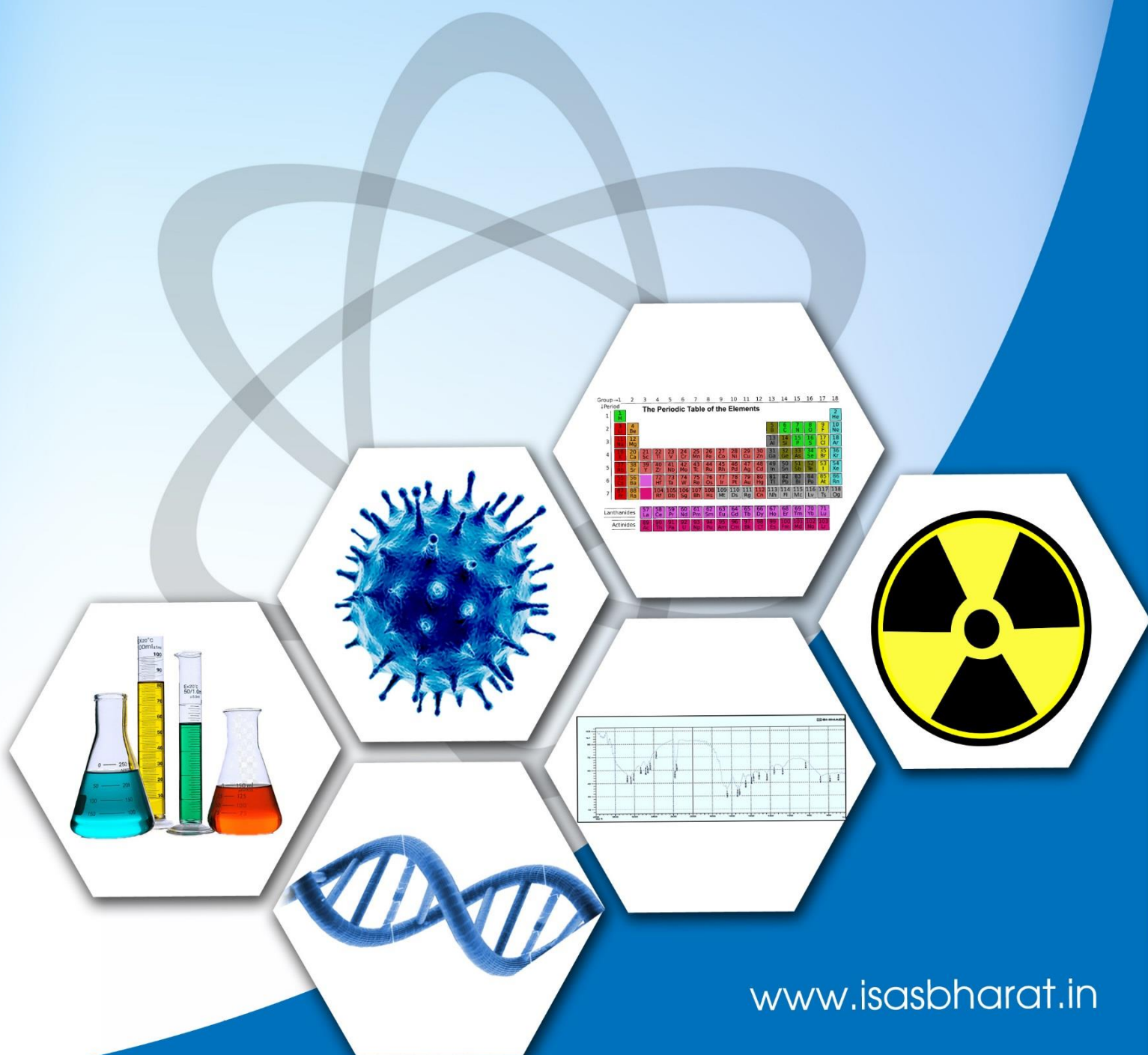




ISSN: 2583-5459
Volume 3 Issue 3
January, 2025

Journal of ISAS

An open access peer reviewed quarterly e-journal by
Indian Society of Analytical Scientists





Journal of ISAS

An open access peer reviewed quarterly e-journal published by Indian Society of Analytical Scientists

Published by: Indian Society of Analytical Scientists (ISAS)

Address: C/o REDS, BARC, Mumbai 400085

Email: isasjournal@isasbharat.in

President ISAS: Dr. Raghaw Saran

J. ISAS

Editorial Board

Editor in Chief

Dr. Nilima Rajurkar, Pune

Members

Dr. Vijayalaxmi C. Adya, Mumbai

Dr. A. K. Basu, Pune

Dr. Vinay Bhandari, Pune

Dr. Avinash Bharati, Nagpur

Dr. Anu Gopinath, Kochi

Dr. Ravin Jugade, Nagpur

Dr. Padmaja S. Vadodara

Dr. Pradeep Kumar, Mumbai

Dr. Prakash Samnani, Vadodara

Dr. Sridhar T. M , Chennai

Dr. S. K. Yadav, Vadodara

Dr. A. N. Garg, New Delhi

Advisory Board

Chairman

Dr. Raghaw Saran, Nagpur

Members

Dr. V. Sivanandan Achari, Kochi

Dr. V. Balaram, Hyderabad

Dr. J. Manjanna, Belgavi

Dr. V. R.Nair, Kollam

Dr. Amrit Prakash, Mumbai

Dr. S. Sriman Narayanan, Vellur

Dr. Shivaramu Prasanna, Bengaluru

Dr. K.P. Vijayalakshmi, Trivandrum

Dr. Mohammed Yusuff K.K., Kochi

Dr. Rajeev Raghavan, Trivandrum

Instruction to Authors

- The Manuscript should be typed in **MS word** (times new roman) with **1.5 spacings** and **font size 12**
- The **title** of the paper should be clear and concise(**font size 14 and bold**), the first letter of each noun and adjective in the title must be in capital letter. It will be followed by names of authors(initials followed by surname) with their affiliation (**font size 12**)
- Corresponding author should be indicated by * with email ID
- The text should be divided into following sections:
 - **Abstract : up to 300 words**
 - **Key words: 5-6**
 - **Introduction**
 - **Experimental**
 - **Results and Discussion**
 - **Conclusions**
 - **Acknowledgement**
- Figures and Tables should be before references with a caption **Figures:** Followed by **Tables:**
- **References**
 - Divisions within the section should be indicated as subheadings
 - The figures and tables should be numbered with Roman numerals and must be mentioned in the text at appropriate places
 - Standard abbreviations for technical terms and journals should be used
 - All constants should be expressed in **SI units**
 - References should be numbered consecutively and should appear in the text as superscript at appropriate places.
 - References should be in following pattern
 - For research paper:**
Authors' initials and surname, Journal abbreviation, Volume, Page, Year.
 - For book:**
Authors' initials and surname, Book name, Publisher, Place, Year.
 - For proceedings:**
Authors' initials and surname Proceedings' of the conference name, place, Page, Month and Year.
- The paper is to be submitted in word file and PDF file to isasjournal@isasbharat.in
- After getting the acceptance of the paper, authors have to submit **signed copyright form and undertaking** before publishing the article



Indian Society of Analytical Scientists.



Editorial

Dear Readers,

It is with great pleasure we present the 11th issue of the *Journal of ISAS (J. ISAS)*, a testament to our commitment to fostering and sharing high-quality research that addresses critical scientific challenges. The journal is quarterly open access e-journal with ISSN and Doi number having free access to all. This issue features a diverse array of contributions, reflecting the multidisciplinary nature of contemporary science.

One of the featured studies explores the degradation of Prazosin, a pharmaceutical pollutant, using innovative dual activity hydrodynamic cavitation reactors. This work offers valuable insights into the development of advanced methods for environmental remediation. Another paper delves into the application of Raman spectroscopy in the study of carbon materials, emphasizing its pivotal role in understanding and characterizing these versatile substances, which are at the forefront of material science and nanotechnology. The issue also includes a fascinating study on the facile synthesis, characterization, and photocatalytic activity of MOF-5, a promising metal-organic framework with significant potential for sustainable energy solutions. Additionally, research focused on the identification and quantification of amino acids in medicinal plants from the Western Ghats, Maharashtra, using High-Performance Thin-Layer Chromatography (HPTLC), adds valuable data to the fields of ethnopharmacology and natural product research.

In addition to these original research articles, this issue features a review of the book "*Textbook of Environmental Education for Undergraduates*," It highlights the book's contribution to

fostering environmental awareness and education, making it an essential tool for undergraduate learning.

The wide-ranging topics in this issue demonstrate the dynamism and depth of contemporary research. These contributions not only expand the boundaries of knowledge but also pave the way for future innovations and practical applications. We extend our heartfelt gratitude to the authors for their exceptional work, the reviewers for their critical evaluations, and the editorial team for their dedication to maintaining the journal's quality and integrity. My special thanks are due to Dr. Raghaw Saran, Dr. Vinay Bhandari and Dr. Vijalalaxmi Adya for their cooperation in bringing this issue. Technical support from Shivani Katak and Vaibhav Parse is duly acknowledged.

We hope this issue inspires our readers to explore new perspectives, engage in meaningful discussions, and contribute to the advancement of science. Your feedback and suggestions are always welcome as we strive to improve and serve the scientific community better.

Thank you

Sincerely



Dr. Nilima Rajurkar

Editor in Chief

J.ISAS

Journal of ISAS

ISSN: 2583-5459 3(3), Pages 1 to 65, (2025)

(An open access Peer reviewed quarterly e- journal by Indian Society of Analytical Scientists)

Contents

S.No.	Title and Authors	Page no.
1	Research Paper: Degradation of Prazosin by using Newer Dual Activity Hydrodynamic Cavitation Reactors Sanjana V. Almeida, Divya Dixit, Dinesh Bhutada, Vinay M. Bhandari *Email: vm.bhandari@ncl.res.in DOI: 10.59143/isas.jisas.3.3.SJPL9246	1-25
2	Review: Raman Spectroscopy in the Research of Carbon Materials Kinshuk Dasgupta Email: kdg@barc.gov.in DOI: 10.59143/isas.jisas.3.3.VZSB5130	26-42
3	Research Paper: Facile Synthesis, Characterization and Photocatalytic activity of MOF-5 Manisha A. Bora*, Suhani Patel, Parag Adhyapak *Email: bmanishabora@gmail.com DOI: 10.59143/isas.jisas.3.3.NGDB1398	43-52
4	Research Paper: Identification and Quantification of Amino Acids in Medicinal Plant Samples from Western Ghats, Maharashtra using HPTLC Technique Vivek Rathod Email: rathod.vivek@live.com DOI: 10.59143/isas.jisas.3.3.BJTE8989	53-63
5	BOOK Review: Textbook of Environmental Education for undergraduates- Edited by Dilip Ganguly and Vikram S. Ghole Dr. Nilima Rajurkar Email: rnilima@rediffmail.com DOI: 10.59143/isas.jisas.3.3.ORDO4134	64-65

Degradation of Prazosin by using Newer Dual Activity Hydrodynamic Cavitation Reactors

Sanjana V. Almeida^{1,2}, Divya Dixit¹, Dinesh Bhutada², Vinay M. Bhandari^{1*}

¹Chemical Engineering and Process Development Division

CSIR-National Chemical Laboratory, Pune-411008, India

²Department of Chemical Engineering, Dr. Vishwanath Karad MIT- World Peace

University, Kothrud, Pune- 411038, India

Email: vm.bhandari@ncl.res.in

Received: 10.12.2024, Revised: 25.1.2025, Accepted: 26.1.2025

Abstract

A study was conducted to investigate the degradation of Prazosin, an Alpha-1 Adrenergic Blocker, which is commonly used in the treatment of Hypertension. The study aimed to achieve improved efficiency using Hydrodynamic Cavitation (HC) and Process Intensification. A new cavitation technique that utilises the Dual Activity Reactor, which is a vortex flow-based cavitation device, was introduced in the study. Two different types of vortex diodes were used in a comparative investigation: a Non-Catalytic Aluminium diode and a Dual Activity Copper diode exhibiting catalytic properties. The impact of pressure on Prazosin degradation and mineralisation was studied on a pilot-plant scale with a capacity of 1 m³/h. Process Intensification was carried out by Aeration, Hydrogen Peroxide, and pH modification. The results showed that aeration produced significant degradation (~18% degradation) using the Cu-Vortex Diode compared to the Al-Diode. The use of H₂O₂ resulted in complete (100%) degradation of the Active Pharmaceutical Ingredient (API) pollutant within just 5 minutes of treatment. Effective mineralisation of ~55% was obtained with the Cu-Diode, whereas only 34% was obtained with the Al-Diode. The development of Hydrodynamic Cavitation technology, with the incorporation of a Dual Activity Reactor-Cu Vortex Diode as a cavitation device, represents a remarkable breakthrough in the field of industrial wastewater treatment. This technology can provide an efficient and practical solution to remove various API pollutants, thereby reducing the environmental impact of industrial activities. The potential benefits of this technology for the industry are immense, opening up a world of possibilities for cleaner and more sustainable industrial practices.

Keywords: *Wastewater Treatment, Degradation, Pharmaceutical, Advanced Oxidation, Technology.*

1.Introduction

Hydrodynamic cavitation (HC), an advanced oxidation process, is considered to be an effective technique in various areas of water, energy, chemicals, and materials sectors. Cavitation here creates a low-pressure region within a cavitation reactor, leading to the formation of vaporous cavities; the bubbles are allowed to grow and collapse in a specified manner. These cavities undergo pressure fluctuations and collapse catastrophically, producing intense shear forces, localized high-pressure and temperature zones (T, ~10000 K and P, ~1000–5000 atm) which results in-situ generation of hydroxyl radicals¹. Hydrodynamic cavitation reactors involve the use of specific designs of cavitating devices, which may or may not incorporate moving parts, and are used in various areas, such as biomass pretreatment², food and beverage processing³, extraction of natural bioactive⁴, microbial disinfection⁵⁻⁷, desulfurization of fuels⁸, removal of refractory pollutants like active pharmaceutical ingredients (APIs)^{9,10}, phenolic compounds¹¹, dyes¹² etc. HC offers numerous advantages over other advanced oxidation processes (AOPs) such as Fenton oxidation, photocatalysis, UV treatment, electrochemical oxidation, and ozonation, for mineralization without secondary waste generation or the use of external catalysts¹³.

Various geometric configurations for hydrodynamic cavitation reactors have been reported, including linear flow devices like venturi and orifice, and non-linear flow devices like vortex diode and rotor-stator assembly. The vortex diode, employing rotational flow offers advantages such as high energy efficiency, low pressure requirements, reduced clogging, and easy scale-up¹⁴. The efficiency of HC processes can be intensified by adding oxidizing agents, nanoparticles, or metal/metal oxides¹³, or by modifying cavitation reactors through changes in the material of construction or by coating the internal surface of the reactor with appropriate metals like copper, nickel, iron, silver¹⁵⁻¹⁶. Parsa et al. reported the catalysed HC process combined with scrap iron sheets as a catalyst for decolorization of Rhodamine B¹⁷. Copper oxide and peroxymonosulfate-activated copper oxide have been reported as highly promising catalysts, in the form of pellets or nanoparticles, to enhance the degradation of various organic pollutants¹⁸⁻²⁰. Recently, dual-activity cavitation reactors combining catalytic activity with

cavitation have shown remarkably high degradation rates for API pollutants such as cephalexin, ciprofloxacin, metformin^{15,16,21}.

Due to the increase in emerging contaminants, particularly from pharmaceutical industries, it is crucial to develop effective methods for removing these refractory pollutants. Prazosin Hydrochloride (PRH), being an Alpha-1 Adrenergic Blocker, is widely used to treat hypertension, benign prostatic hyperplasia, and post-traumatic stress disorder. Due to its extensive use, PRH finds its way into the environment through various channels, such as the disposal of medicines through healthcare centres, industrial effluent, and human feces. Al-Qaim reported the typical concentrations of prazosin in influent sewage treatment plants (14-525 ng/L) and raw leachate (3850 ng/L)²³⁻²⁴. The rapid growth of the pharmaceutical industry, coupled with widespread medication usage, leads to elevated levels of API pollutants in industrial wastewater and in surface waters. This necessitates the development of suitable treatment technologies or modifications to ensure a sustainable and economically viable approach for treating effluents containing low to high concentrations.

Very few methods for the removal of PRH have been reported so far that include different advanced oxidation processes such as electrochemical oxidation²⁵⁻²⁶, activated sludge process using aerobic sequencing batch reactor (SBR)²⁷, biodegradation²⁸, photocatalysis²⁹, stress conditions³⁰. Mussa et al. reported the electrochemical oxidation of different therapeutic classes of pharmaceuticals, including PRH, using a graphite PVC composite electrode, achieving 98% degradation in 50 minutes of electrolysis²⁶. Al-Qaim also reported 96% PRH degradation using an electrochemical degradation process in NaCl medium in 40 minutes²⁵. Other than these methods, biodegradation of prazosin was also reported by isolating and characterising the potential microbes that help in the degradation process, resulting in 88% of the removal rate²⁸. Bakshi et al. demonstrated that PRZ underwent significant degradation under hydrolytic stress³⁰. Zaini et al. reported the removal of PRH using the aerobic sequencing batch reactor system and found moderate degradation efficiency of 41%²⁷. Despite many reported methods achieve high removal rates (~98%), these have significant drawbacks such as high maintenance costs, high energy requirements, secondary waste generation, the formation of numerous by-products, and high treatment times. It is intuitive to develop a cost-effective and techno-economically feasible technology to degrade PRH with for industrial scale applications.

The present study demonstrates remarkably high degradation rates for prazosin by hydrodynamic cavitation. Two different vortex diodes were used: Al-vortex diode and Cu-vortex diode. The studies were carried out on a pilot plant scale with a capacity of 1 m³/h. The methodology suggests potential for redesigning reactors in the existing cavitation processes by changing the material of construction (MOC) using selected catalytic metals. It promises significant improvements in the removal efficiency and for lowering treatment costs.

2. Materials and Methods

2.1 Materials

Prazosin Hydrochloride (C₁₉H₂₁N₅O₄.HCL; 419.86 g/mol; CAS: 19237-84-4; Purity > 99.9%, BLD Pharma Pvt Ltd, India) in crystalline form was used to prepare synthetic wastewater. The chemical and physicochemical properties of PRH are listed in Table 1. Hydrogen Peroxide (H₂O₂; 50% w/v, AR grade, RANKEM, Mumbai) and Acetonitrile (≥ 99.9% Purity, HPLC grade, Avantor Performance Materials) was used for the process intensification studies. pH modification was performed using 1N Nitric acid (70% w/v) and 1N Sodium hydroxide, both procured from Merck, India.

2.2 Experimental Methodology

The hydrodynamic cavitation pilot plant setup with a capacity of 1 m³/h was used to study the degradation of prazosin (Fig. 1). The methodology was already described in our previous research^{9,15} and hence only the essential details are discussed here.

The pilot plant setup consisted of a 50 L water storage tank and a multistage centrifugal pump (Model CNP, CDLF2–26, SS316, 1.2 m³/h at 228 MWC, power rating 3 kW (4 hp), India) for pumping the wastewater. Two vortex diodes, each having an 11 mm throat diameter and a 66 mm chamber diameter, were utilized as cavitation reactors. One was a conventional aluminum vortex diode, and the other was a dual-activity catalytic reactor, a copper vortex diode, which exhibits additional catalytic activity. The pressure drop across the cavitation reactor was adjusted and measured using pressure transmitters (Honeywell ST 700, India). A flow transmitter (KRONE, H250) with a range of 150–1500 LPH and an integral analog indicator was used to measure the mainline flow rate while a thermocouple-RTD (EUREKA Eng.

Enterprises India; 0–200°C) was used to measure the inlet temperature of the system. The temperature within system was controlled by a cooling system (JULABO, Model FL 1701, Japan). The entire setup was mounted on a stainless-steel frame with wheels.

All the experiments were performed with 20 L synthetic wastewater containing a known initial concentration of 10 mg/l prazosin. The effect of pressure drop was studied in the range of 0.5–2 bar across the vortex diode. The aeration effect on PRH degradation was studied by bubbling air into the wastewater tank using an air pump (SOBO AQUARIUM SB-9905). Additionally, the process intensification was carried out using hydrogen peroxide at different molar ratios of PRH: H₂O₂ such as 1:100 (0.081 g/L), 1:200 (0.162 g/L) and 1:500 (0.405 g/L). The effect of pH was studied by modifying the pH of the wastewater solution under acidic (pH 4) and alkaline conditions (pH 9). All the experiments were carried out for 60 minutes, with samples withdrawn at intervals of 5–10 minutes. The reproducibility of the experiments was confirmed and found to be satisfactory.

2.3 Analysis

The analysis for the removal of the model API pollutant-Prazosin was carried out using Total Organic Carbon (TOC-L-H564054; Shimadzu, Japan) and High-Performance Liquid Chromatography (HPLC, Prominence i-series LC2030c 3D plus HPLC, Shimadzu C-18 Column, 4.6 × 250 mm, particle size 5 µm). The mobile phase consisted of acetonitrile (75%) and 0.1% formic acid in deionized water (25%), used as the eluent for detecting Prazosin at a flow rate of 1 ml/min and a wavelength of 247 nm. The pH of the samples was measured using a Multi Para MP-5 pH meter (Spectra Lab Instruments Pvt. Ltd., India). The determination of intermediates formed during prazosin degradation was conducted through Liquid Chromatography High-Resolution Mass Spectroscopy (LC-HRMS) analysis.

3. Results and discussion

3.1 Effect of pressure drop on the degradation of PRH

Pressure drop across the cavitation reactor is a decisive parameter for the efficiency of the treatment. As in earlier findings, the cavitation inception point for vortex diode was found to be ~0.48 bar pressure drop and therefore, the pressure range for the pressure drop was selected

as 0.5–2 bar to find optimum pressure drop⁸. It may be noted that the degradation decreases or remains constant beyond the optimum point due to possible super cavitation phenomenon which eventually reduces the cavitation intensity¹³.

The results from Figure 2 clearly show a significantly higher degradation of PRH at optimum pressure drop of 0.5 bar, which then decreases, indicating no requirement of high pressures beyond the pressure drop of 0.5 bar. A maximum degradation of 31% and 35% of PRH was achieved using the Al-vortex diode and Cu-vortex diode, respectively. In comparison, TOC reduction of 30% using the Cu-vortex diode was approximately twice that of the Al-vortex diode at 0.5 bar ΔP , indicating additional catalytic action of Cu metal. From Fig. 3 (a, b), the HPLC results indicate that there is no intermediate formation for only HC process. The kinetics of PRH degradation was evaluated using a pseudo-first-order reaction by equation 1, and the kinetic constant values for vortex diodes are listed in Table 2.

$$C = C_0 e^{-kt} \quad (1)$$

Where, C_0 and C are the PRH concentrations initial and final concentration. ‘ t ’ is time in min and ‘ k ’ is the first order rate constant (min^{-1}). For the optimum pressure drop, ΔP , of 0.5 bar, the corresponding k values for the Al-vortex diode and Cu-vortex diode were $6.2 \times 10^{-3} \text{ min}^{-1}$ and $7.2 \times 10^{-3} \text{ min}^{-1}$, respectively.

Many researchers have investigated the effect of pressure drop on the degradation of pollutants, suggesting that significantly higher-pressure drops are required for other cavitation reactors than vortex diodes. However, the optimal pressure drop depends on the reactor configuration and the type of pollutants involved^{9,31}. Raut-Jadhav reported a maximum degradation of 27.49% for the methomyl pesticide using hydrodynamic cavitation with a circular venturi having a 2 mm throat diameter, at a very high inlet pressure of 3 bar³¹. However, for the degradation of imidacloprid insecticide, a very high inlet pressure of 15 bar was required to achieve a 26.5% degradation³². Dixit et al. reported the superiority of the vortex diode over the orifice plate as a cavitation reactor by comparing the degradation efficiency of the naproxen compound. The orifice device required a very high pressure drop of 5 bar, more than three times than that required by the vortex diode⁹.

The degradation of only 31-35% is not sufficient for industrial applications. Consequently, the improvement by catalytic devices needs further investigation through process intensification or modifications in hydrodynamic cavitation.

3.2 Effect of aeration on PRH degradation combined with HC

Introducing gases like air, oxygen, or ozone can significantly influence cavitation by affecting the number and behaviour of bubbles. Air, being cost-effective, is beneficial for process intensification. It enhances cavitation by promoting gas or vapor nuclei formation and supporting oxidation reactions through oxygen, which increases oxidizing species and, consequently, the degradation of pollutants. For evaluating synergism between the combined approach of HC and aeration, experiments were conducted at similar operating conditions, such as a constant initial concentration of 10 ppm and a pressure drop of 0.5 bar by continuously bubbling air to a recirculating tank. It was observed (Fig. 4) that the extent of degradation of PRH increases from 31% to 39% with a 26% TOC reduction, and from 35% to 46% corresponding to 35% TOC reduction through intensified process of HC and aeration using the Al-vortex diode and Cu-vortex diode, respectively. The results also indicate a higher rate of degradation due to the enhancement in the kinetic rate constant of HC + aeration compared to HC alone, confirming synergism (Table 2). The synergistic index (ξ) for the combined process of HC and aeration was calculated using equations 2 and 3 for both vortex diodes.

$$\xi_{Al-vortex\ diode} = \frac{k_{HC+aeration}}{k_{HC} + k_{aeration}} = \frac{8.3 \times 10^{-3}}{6.2 \times 10^{-3} + 0} = 1.34 \quad (2)$$

$$\xi_{Cu-vortex\ diode} = \frac{k_{HC+aeration}}{k_{HC} + k_{aeration}} = \frac{10.3 \times 10^{-3}}{7.2 \times 10^{-3} + 0} = 1.43 \quad (3)$$

The synergistic index values of 1.34 and 1.43, greater than 1, indicate good synergism and highlight improvement in the efficiency of the combined HC and aeration process compared to the individual processes.

Many literature studies have reported aeration as a process intensification approach in the hydrodynamic cavitation for higher efficiency in wastewater treatment applications. Bokhari et al. reported achieving 90% degradation of benzene at an inlet pressure of 3 bar within 50 minutes using a combined approach of HC and aeration³³. Patil et al. observed a 100% improvement in the degradation of octanol solvent by employing an aeration-based process

intensification method. Nevertheless, the authors pointed out that this enhancement was not effective for degrading other chemicals like metformin, ciprofloxacin, DMF and cyclohexanol³⁴⁻³⁶. While aeration is expected to enhance oxidation by increasing oxidizing species, its impact on degradation rates varies with pollutant characteristics. Thus, aeration's effectiveness is pollutant-specific and minimally affected by device or process conditions. The pollutant's nature is the key factor in leveraging aeration-based intensification.

3.3 Effect of H₂O₂ addition on PRH degradation in combined with HC

Hydrogen peroxide acts as a strong oxidizing agent and the addition of H₂O₂ to hydrodynamic cavitation process increases the generation rate of hydroxyl radicals (OH•), which, if used effectively, can significantly intensify the breakdown of organic pollutants¹³. The effect of H₂O₂ at different loadings was examined, with molar ratios of PRH to H₂O₂ set at 1:100, 1:200, and 1:500. Like conventional intensification methods, the newer catalytic cavitation process can also be enhanced, offering additional benefits due to improved catalytic activity. The experiments were conducted using both Al and Cu-vortex diodes under the same conditions of a pressure drop (ΔP) of 0.5 bar and a concentration of 10 ppm. The extent of PRH degradation obtained for different molar ratios of PRH:H₂O₂ is shown in Fig. 5.

It was observed that a complete degradation of PRH with 37% TOC reduction was achieved using the Cu-vortex diode within 5 minutes by using low molar concentration of H₂O₂, 1:100 molar ratio. Whereas, with the Al-vortex diode, the extent of degradation increased from 83% to 100% within 5 minutes as the H₂O₂ loading increased from a 1:100 to 1:500 molar ratio. Fig. 3 (c, d) illustrates the HPLC analysis of PRH degradation using HC and H₂O₂, where a single peak for PRH was observed, indicating no formation of by-products during process intensification. The degradation profile shows a predominant mineralization pathway, with water and carbon dioxide as the sole products. By increasing the H₂O₂ loading to a 1:200 ratio, TOC reduction for the Cu-vortex diode increased to 55%. However, further increases in H₂O₂ loading decreased TOC reduction due to the scavenging action of residual H₂O₂. When H₂O₂ loading exceeds the optimal level, the generated hydroxyl radicals react with H₂O₂ as shown in the following reaction³⁷:



This scavenging phenomenon is also confirmed by literature reports, although different optimum values for H₂O₂ loading have been observed. Mishra et al. reported the degradation of Rhodamine B using the combined effect of HC and various H₂O₂ loadings, ranging from 10 mg/L to 200 mg/L. They found that Rhodamine B degradation improved steadily, reaching 99.9% with 200 mg/L H₂O₂, accompanied by a 55% reduction in TOC³⁸.

The degradation rate constants were determined to be $460.5 \times 10^{-3} \text{ min}^{-1}$ for the Al-Vortex diode and $921 \times 10^{-3} \text{ min}^{-1}$ for the Cu-Vortex diode using an optimum dose of a 1:200 molar ratio of PRH to H₂O₂. Thus, process intensification with H₂O₂ resulted in enhancements of over 70 and 127 times compared to HC alone. This indicates that the Cu-Vortex diode achieved a higher degradation rate than the Al-Vortex diode under the same conditions, further highlighting the effectiveness of the Cu-Vortex diode and the synergistic effect of hydrogen peroxide in enhancing PRH degradation. The synergistic index was again calculated as per the calculations shown in following equation 5 and 6:

$$\xi_{Al-HC+H_2O_2} = \frac{k_{Al-HC+H_2O_2}}{k_{Al-HC} + k_{H_2O_2}} = \frac{460.5 \times 10^{-3}}{6.2 \times 10^{-3} + 1.8 \times 10^{-3}} = 57.56 \quad (5)$$

$$\xi_{Cu-HC+H_2O_2} = \frac{k_{Cu-HC+H_2O_2}}{k_{Cu-HC} + k_{H_2O_2}} = \frac{921 \times 10^{-3}}{7.2 \times 10^{-3} + 1.8 \times 10^{-3}} = 102.33 \quad (6)$$

The values of the synergistic indices were observed as 57.56 and 102.33 for Al-vortex diode and Cu-vortex diode, respectively, which confirms the very good synergism of the combined approach of HC and H₂O₂. In the case of the Cu-vortex diode, an exceptionally high synergistic index was observed. This is due to the catalytic action of the modified cavitation reactor. Dixit et al. also reported the similar and high synergistic index values for dual functional cavitation reactor for the degradation of various API pollutant such as cephalexin, ciprofloxacin and metformin.^{15,16,21}. Thanekar et al. reported the 53% enhancement in degradation of carbamazepine with 60% degradation using process intensification through (1:5) H₂O₂³⁷. While the role of H₂O₂ has been established, the optimum loading of H₂O₂ largely depends on the nature of the pollutants in wastewater, highlighting the need for experimental investigation. Additionally, the Cu-vortex diode exhibits remarkable superiority in synergism over the Al-vortex diode due to this material change to catalytic material. It is anticipated that this innovative approach could substantially enhance the conventional cavitation processes.

3.4 Effect of pH on PRH degradation

The effect of pH on the extent of PRH degradation was investigated under varying conditions, specifically acidic (pH 4) and basic (pH 9), using the two vortex diodes as cavitating devices operated under similar optimized conditions. The pH of the medium influences the state of the pollutant molecule (molecular or ionic state), resulting in a change in the degradation pathway of pollutants. In general, the molecular form of a compound is more susceptible to degradation. Therefore, acid dissociation constant (pKa) values can indicate the influence of pH on the degradation process. The pKa values of prazosin HCl are 11.09 and 13.32, indicating that the compound predominantly exists in its molecular form at acidic pH. This suggests that prazosin HCl is more likely to degrade in acidic environments. To establish acidic and basic conditions, pH adjustments were carried out using 1 M Nitric Acid (HNO₃) solution and 1 M Sodium Hydroxide (NaOH) solution, respectively. From the experimental results, a complete degradation of PRH was observed with rate constants of 115.1 x 10⁻³ min⁻¹ for the Al-vortex diode and 921 x 10⁻³ min⁻¹ for the Cu-vortex diode under acidic condition (pH 4). The rate constants surged by over 17 times for the Al-vortex diode and 127 times for the Cu-vortex diode, demonstrating a substantial improvement in the degradation rate and highlighting the superior effectiveness of catalytic cavitation reactors compared to conventional reactors. A maximum TOC reduction of 35% was observed for the Al-vortex diode, whereas the Cu-vortex diode achieved a TOC reduction of 41% under acidic conditions (Fig. 6). The effectiveness of process intensification through pH modification was quantified by calculating the synergistic index values using equations 7 and 8 as follows:

$$\xi_{Al-pH4} = \frac{k_{Al-HC+pH4}}{k_{Al-HC} + k_{pH4}} = \frac{115.1 \times 10^{-3}}{6.2 \times 10^{-3} + 0.3 \times 10^{-3}} = 17.7 \quad (7)$$

$$\xi_{Cu-pH4} = \frac{k_{Cu-HC+pH4}}{k_{Cu-HC} + k_{pH4}} = \frac{921 \times 10^{-3}}{7.2 \times 10^{-3} + 0.3 \times 10^{-3}} = 122.8 \quad (8)$$

Significantly high values of 17.7 and 122.8 were achieved for the process intensification approach through pH modification for both vortex diodes. This confirms the excellent synergistic effect over the Al-vortex diode and surpasses individual approaches.

At basic pH, negligible degradation was observed because the PRH molecule becomes hydrophilic due to ionization. This increases the difficulty of degradation, as hydroxyl radicals

are short-lived, making it less likely for the pollutant to degrade in the bulk solution. These findings indicate that acidic conditions significantly enhance the degradation of prazosin using HC, especially with the Cu-vortex diode. The HPLC analysis showing only one prominent peak of PRH confirmed that no intermediate formation occurred during the degradation of PRH (Fig. 3(e, f)).

The enhancement in PRH degradation clearly demonstrates that pH is a critical operating parameter in the HC process for degrading API pollutants. Various studies have reported the effect of pH on the degradation of different compounds, including dyes³⁸, pesticides³¹, and API pollutants^{15,21,34,35}. Saharan et al. reported that in the HC process, the degradation mechanism includes either the thermal or pyrolytic breakdown of the pollutant trapped inside the cavity, or the reaction of hydroxyl radicals with the pollutant molecules at the gas-liquid interface and throughout the bulk solution³⁹. Patil et al. reported the effect of pH on metformin degradation, achieving a significant enhancement of 3000% with 88% degradation in 180 minutes using a conventional vortex diode with process intensification through pH modification³⁴, whereas Dixit et al. enhanced the degradation of same compound and achieved complete degradation within 5 minutes using Cu-coated cavitation reactor, confirming the effectiveness of dual-functional cavitation reactors with process intensification through pH modification²¹. Mishra et al. found that using a combination of HC and pH modification, acidic conditions significantly enhanced the degradation of Rhodamine B, achieving 59.3% degradation at pH 2.5. Degradation was considerably lower under alkaline and neutral conditions. This is because acidic conditions favor the generation of hydroxyl radicals, reducing radical recombination and increasing their availability for pollutant oxidation³⁸. Therefore, it is clear that the optimal pH condition is specific to each pollutant and must be investigated for various pollutants and operating conditions.

3.5 Per-Pass Degradation & Cavitation Yield Calculation

Conventional kinetic analysis often uses the power-law model, but the per-pass degradation model for HC offers a more detailed view of physicochemical behavior, including flow dynamics, pressure drops, performance of cavitation process, and energy dissipation. It also more accurately assesses the performance of the cavitation process by evaluating cavitation yield, offering a more realistic perspective as it considers concentration effects and pressure

drops within the cavitation device making it particularly suitable for scale-up in large-scale operations.

The per-pass degradation factor (ϕ) was calculated by equation 9¹³:

$$\text{Per - pass degradation factor } (\phi) = \text{Residence time} \times \text{Rate constant} \quad (9)$$

Here, the residence time can be further defined as the volume ratio of the holding tank and the flow rate.

The per-pass degradation factor was calculated for all processes, including process intensification approaches such as aeration, optimised H₂O₂ loading and pH modifications and for both the vortex diodes. The obtained values are shown in Fig. 7 (a). The significant enhancement in the per-pass degradation factor for the Cu-vortex diode can be clearly attributed to its additional catalytic activity. Only marginal improvements were observed with the combined approach of HC and aeration, yielding per-pass degradation factor values of 0.027 for the Al-vortex diode and 0.034 for the Cu-vortex diode, compared to 0.020 and 0.023 for the HC-only process, respectively. In contrast, a significant enhancement was achieved using a process intensification approach with the addition of H₂O₂ at a 1:200 molar ratio, resulting in a 75-fold increase for the Al-vortex diode (1.53) and a 114-fold increase for the Cu-vortex diode (2.30) in the per-pass degradation factor. Similarly, combining acidic pH with HC led to an 18-fold increase for the Al-vortex diode (0.38) and a 114-fold increase for the Cu-vortex diode (2.30). The significant improvements observed with Cu-vortex diode further support the potential use of novel dual-function reactors in wastewater treatment.

Another important factor, the cavitation yield was calculated for the degradation of prazosin, for the different processes and for both the cavitation reactors. The cavitation yield (Y) was calculated using equation 10¹³,

$$\text{Cavitation Yield } (Y) = \frac{\text{Amount of Prazosin degraded}}{\text{Energy dissipation}} \quad (10)$$

The values of cavitation yields obtained for different process alterations have been depicted in Fig. 7 (b). Very low values of cavitation yield, 0.0035 mg/J and 0.004 mg/J, were observed for the only HC process, while minimal improvements were noted with values of 0.0044 mg/J and 0.005 mg/J for the Al and Cu-vortex diodes, respectively. Higher cavitation yields of 6.8×10^{-2} mg/J and 13.6×10^{-2} mg/J were obtained using HC with (1:200) molar ratio H₂O₂, indicating an 18-fold and 33-fold enhancement for the Al and Cu-vortex diodes, respectively.

Similarly, for process intensification approach with acidic condition yield the cavitation value of 1.7×10^{-2} mg/J for Al-vortex diode and 13.6×10^{-2} mg/J for Cu-vortex diode. The results indicate that exceptionally high cavitation yields can be achieved by using a dual-function cavitation reactor with a simple change in the reactor's material, selected based on the nature of the reaction.

Per-pass degradation and cavitation yield are interrelated terms and reflect the effectiveness of the cavitation process and various process intensification. Both parameters are important for understanding the hydrodynamic cavitation, analyzing and comparing literature data, and future research on different devices. While the per-pass degradation factor is particularly useful for scaling up hydrodynamic cavitation, cavitation yield is more pertinent for assessing the energy efficiency of the process.

3.6 Cost analysis

The cost is a crucial factor for adopting any process for real life application, including new cavitation technologies. Energy required for pumping during hydrodynamic cavitation is a major cost component. Thus, the economics of cavitation processes must be thoroughly evaluated, especially in comparison to conventional methods. The treatment cost using HC process can be calculated by equation 11:

$$\text{Cost of treatment per } m^3 \text{ of effluent} = \frac{N_c \times \Delta P \times P_E}{36\eta} \quad (11)$$

where, N_c is the number of passes, ΔP is the pressure drop across the cavitation reactor, P_E is the cost electricity, η is the pump efficiency (66%) for commercial usage. Electricity was assumed to cost 10 Rs/kW·h.

With a vortex diode operating at an optimal pressure drop of 0.5 bar for 60 minutes, the cost for hydrodynamic cavitation alone was 0.044 \$/m³, resulting in only a 15–30% reduction, which limits its practical use. For industrial wastewater treatment, complete degradation is desired. The cost was significantly reduced to approximately 0.0049 \$/m³, about 10 times lower, when using both vortex diodes with process intensification through the addition of H₂O₂ at a 1:200 molar ratio. Similarly, a simple acidic pH adjustment significantly reduced

the treatment cost. Cost analysis for the combined HC+ pH 4 process showed treatment costs of 0.029 \$/m³ for the Al-vortex diode and 0.0049 \$/m³ for the Cu-vortex diode. The modified hybrid approach using a dual functional vortex diode with hydrogen peroxide, or pH adjustment provides an efficient and cost-effective alternative for PRH degradation. This method offers superior cavitation yield and high efficiency. The dual-activity cavitation reactor highlights the importance of reactor design and process intensification in reducing treatment time and costs.

Conclusions

The present study demonstrated, for the first time, the effective use of hydrodynamic cavitation with vortex diode, more specifically dual activity vortex diode, as a cavitating device for degrading prazosin for exceptional enhancement in the rate of degradation and extraordinarily high cavitation efficiency. The important findings are:

1. HC alone for the degradation of PRH resulted in a limited 15-30% reduction, with a maximum TOC reduction of 35% at 0.5 bar pressure drop. Combining HC with H₂O₂ achieved complete degradation in 10 minutes for the Al-vortex diode and in 5 minutes for the Cu-vortex diode, at a (1:200) molar ratio loading.
2. The pH has significant impact and an acidic pH of 4 was found best for PRH degradation in both reactors. Complete degradation was observed within 5 minutes using the Cu-vortex diode, while the Al-vortex diode required 40 minutes.
3. Exceptionally high synergism was observed, with synergistic index values of 57.56 and 102.33 for process intensification using H₂O₂, and 17.7 and 122.8 for the combined approach of HC and acidic pH, for the Al and Cu-vortex diodes, respectively.
4. The per-pass degradation model demonstrated a remarkable improvement of approximately 114 times using the Cu-vortex diode with process intensification approaches, confirming its superiority over the conventional Al-vortex diode, which showed an 18-75 times improvement.
5. The process intensification approaches of using H₂O₂ or modifying the acidic pH highlight a 3300% enhancement for the Cu-vortex diode, compared to a 300-1800% improvement for the Al-vortex diode.

The results confirm that using a newer vortex flow-based device in hydrodynamic cavitation, combined with process intensification through H₂O₂ or acidic pH conditions, leads to significant degradation of PRH with a low treatment cost. The methodology, therefore, can provide a techno-economical alternative for the degradation of PRH and wastewater treatment.

Acknowledgement

The author-VMB wishes to acknowledge the financial support from Water Innovation Center-Technology, Research and Education (WICTRE) (DST/TM/WTI/WIC/2K17/100(G)), of Department of Science and technology, Ministry of Science and Technology, India and also financial support from Council of Scientific and Industrial Research (CSIR), Government of India (MLP102326).

Figures:

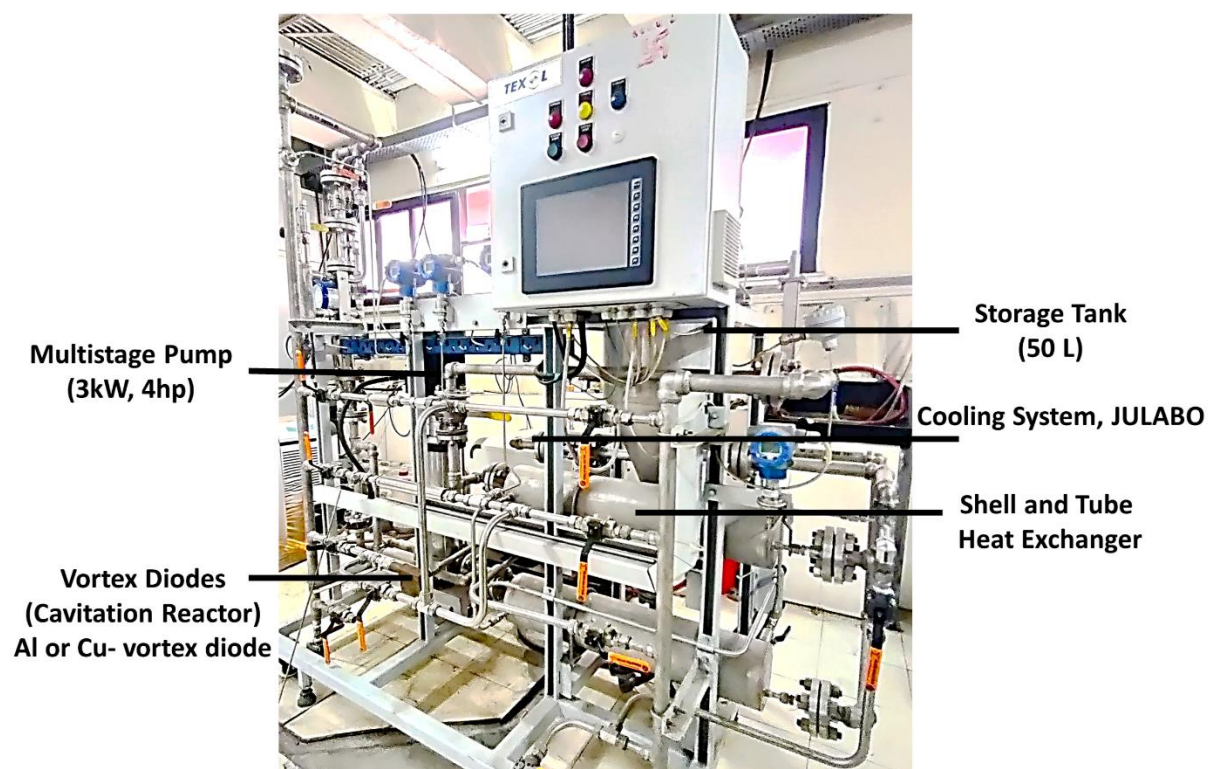


Fig. 1. The hydrodynamic cavitation experimental set-up

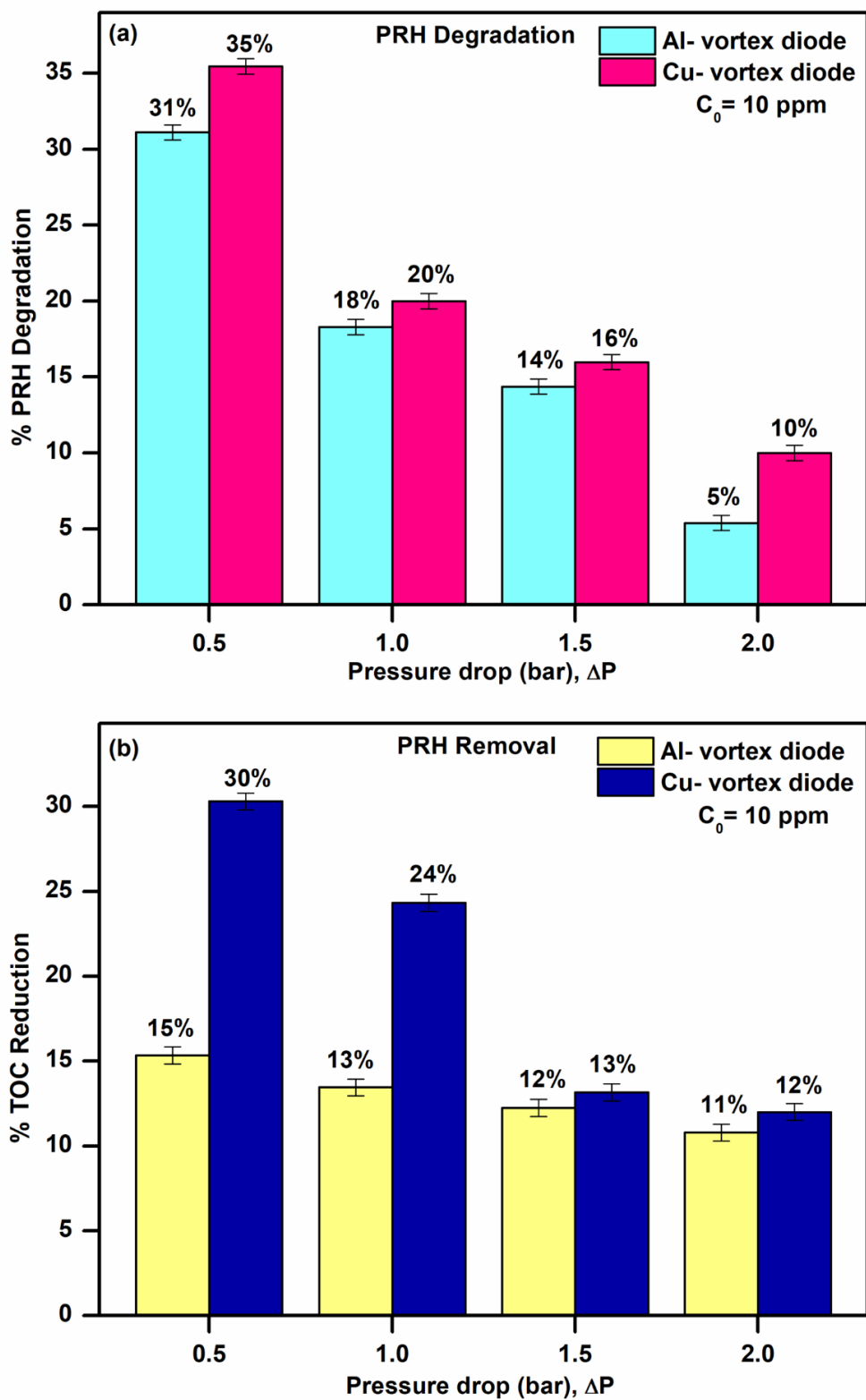


Fig. 2. Effect of pressure drop on degradation of PRH using Al and Cu-vortex diode

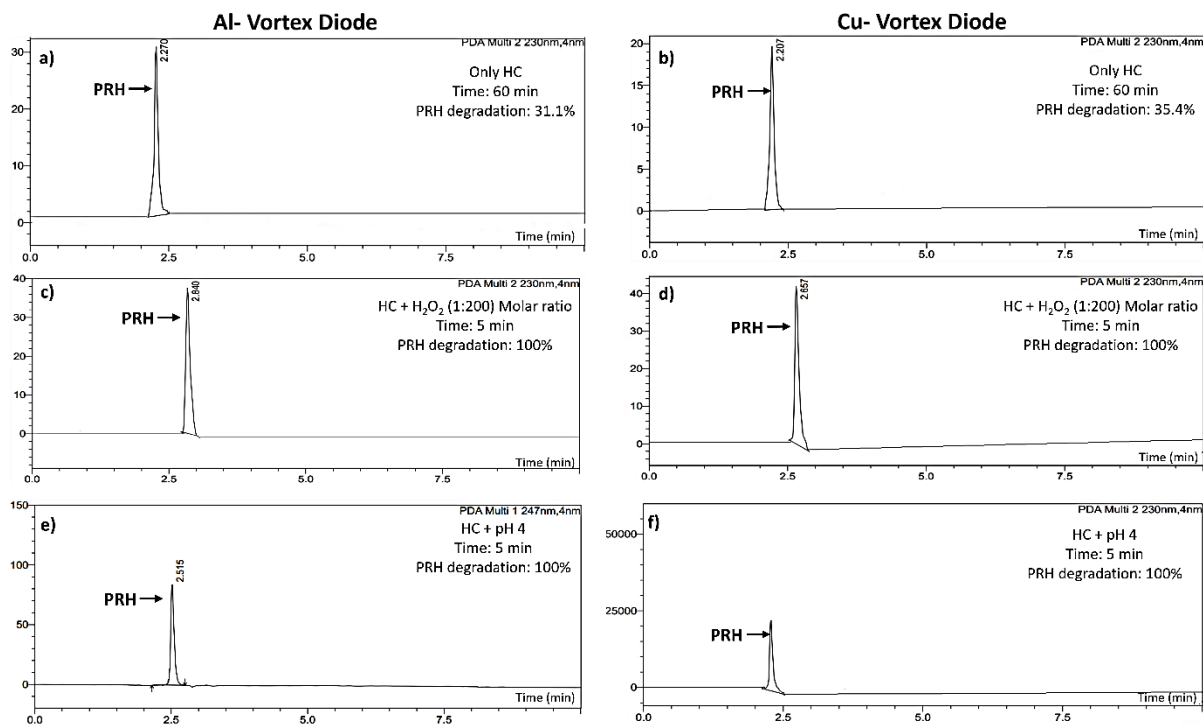


Fig. 3. HPLC analysis of different treatment approaches using both vortex diodes

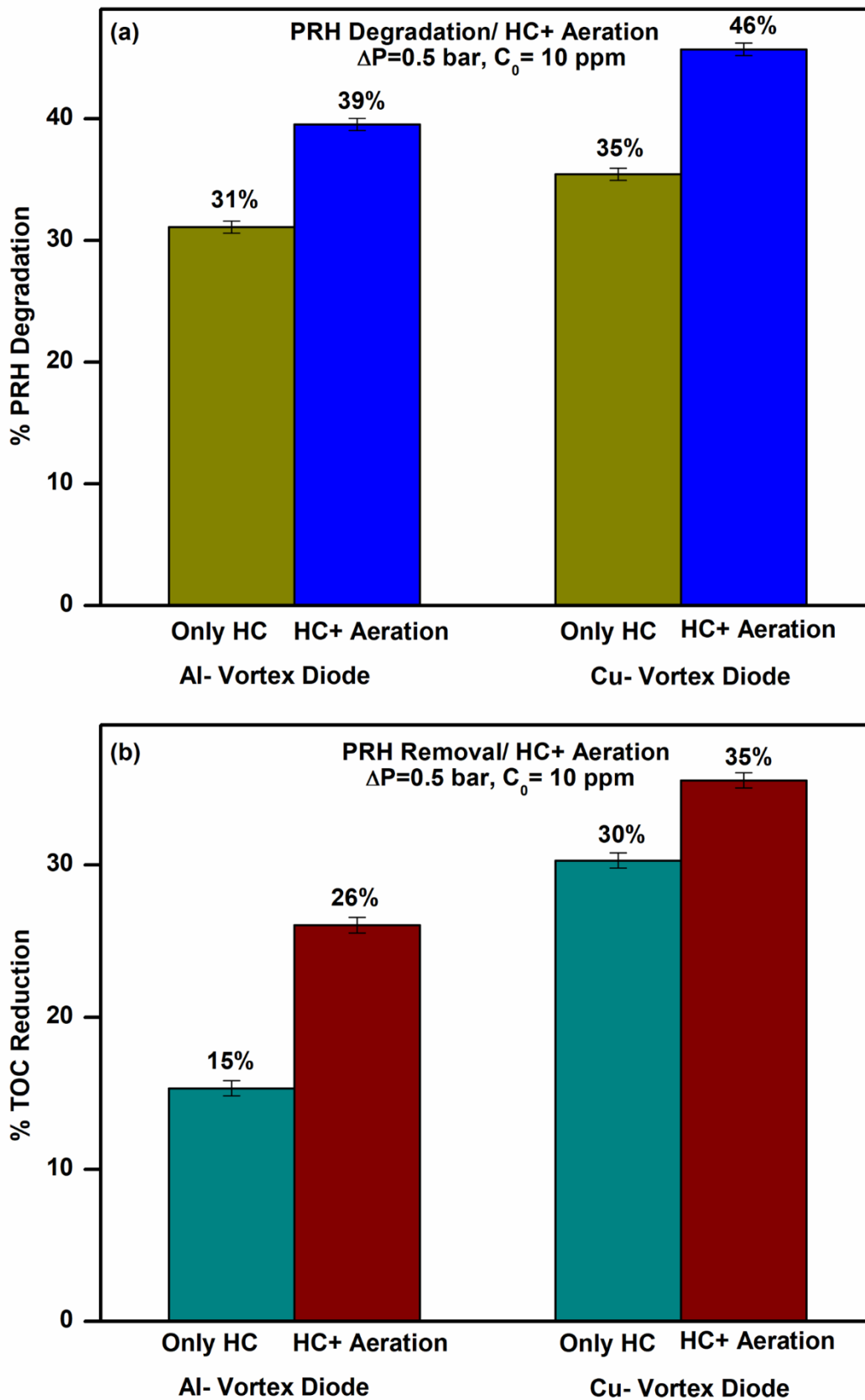


Fig. 4. Effect of aeration on PRH degradation combined with HC

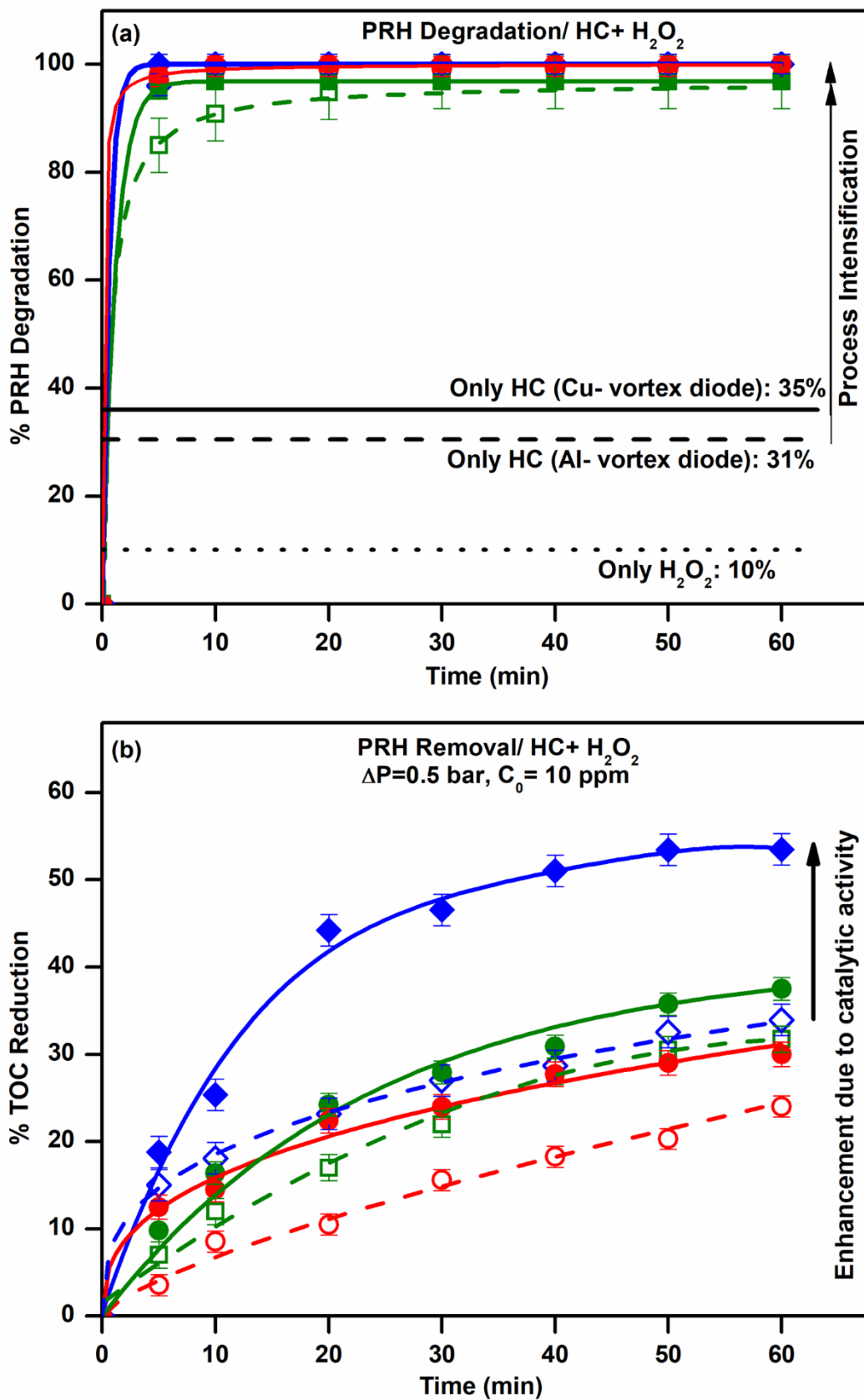


Fig. 5. Degradation of PRH using process intensification approach of H₂O₂

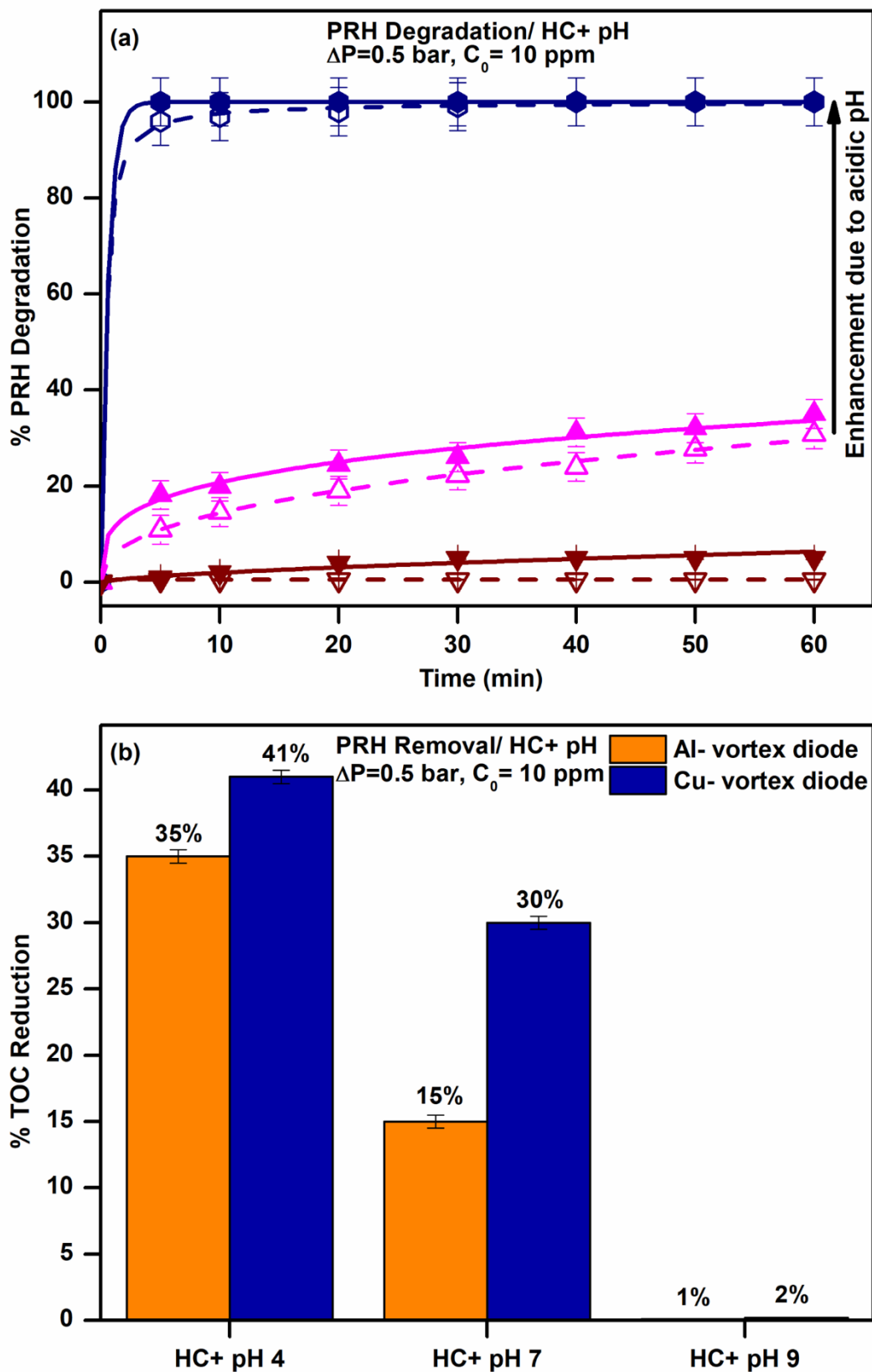


Fig. 6. Degradation of MTF using combined approach of HC and pH

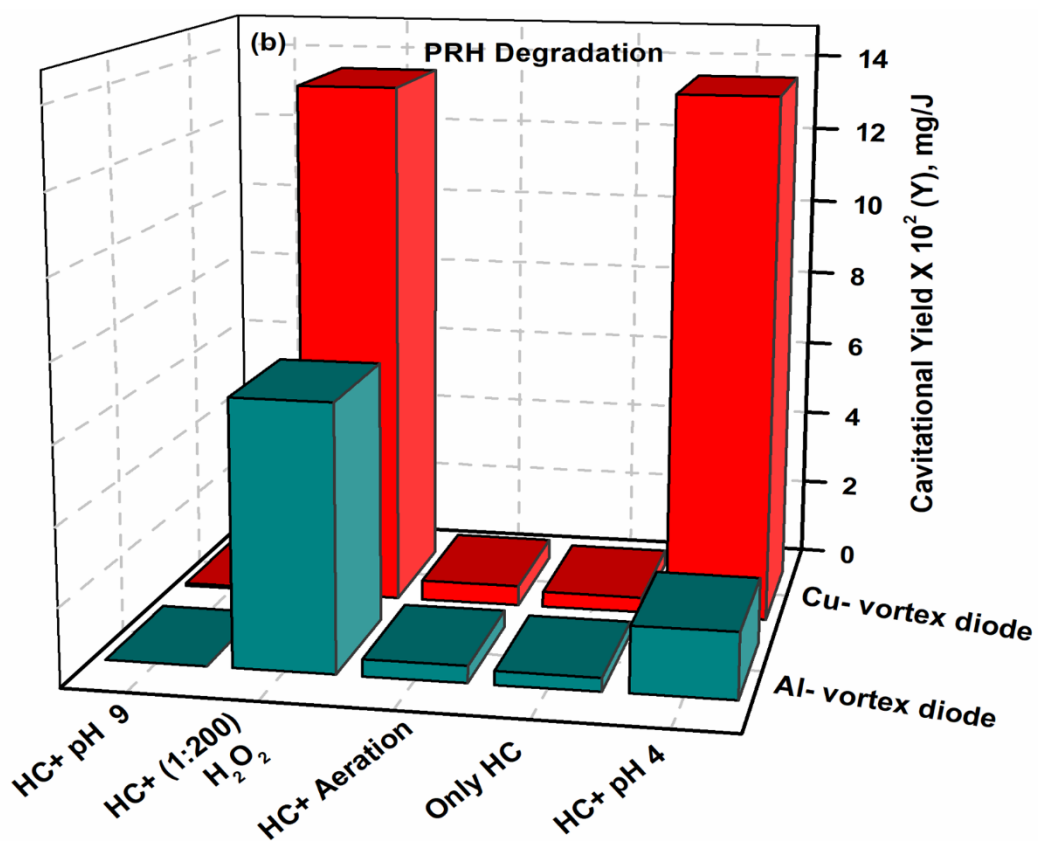
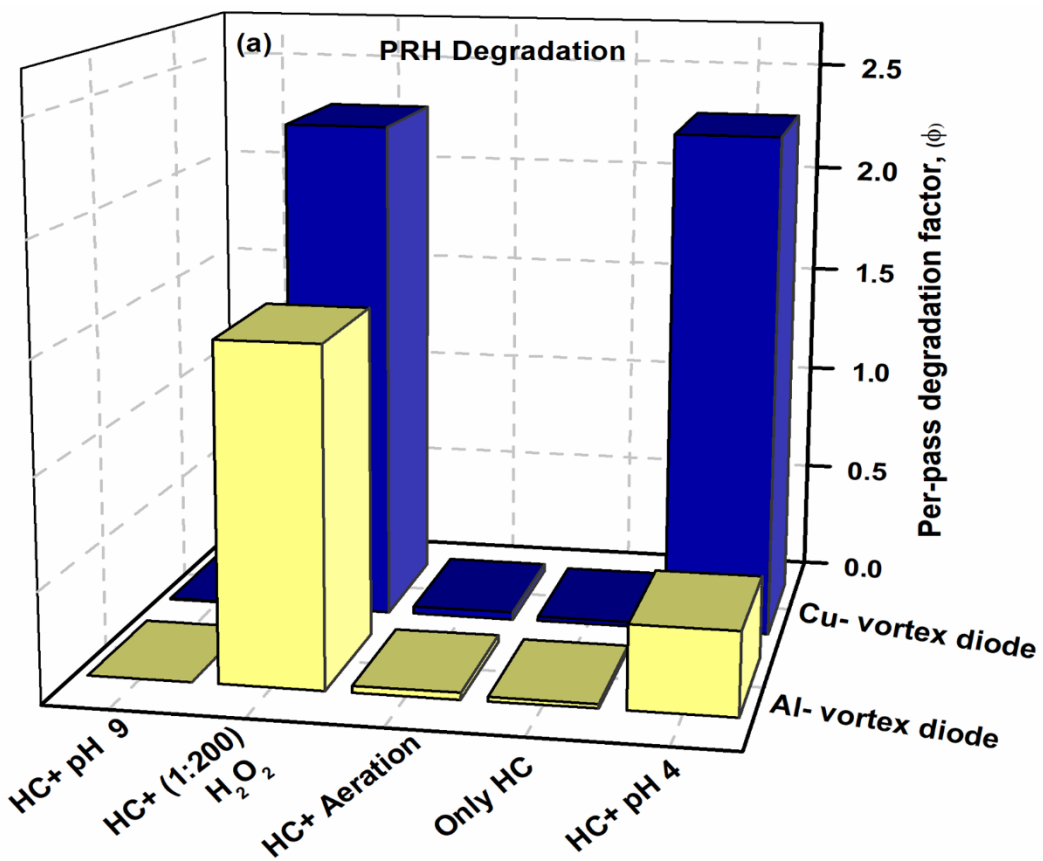


Fig. 7. Per-pass degradation and cavitation yield for PRH degradation

Tables:

Table 1. Chemical and Physicochemical Properties of Prazosin

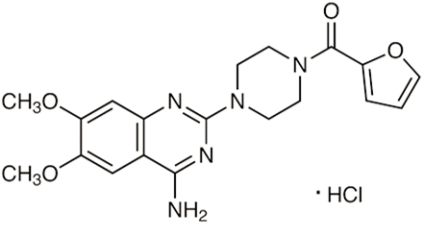
Structure	Name	Prazosin HCl
 <p>CH₃O CH₃O NH₂ · HCl</p>	IUPAC name	1-(4-Amino-6,7-dimethoxy-2-quinazolinyl)-4-(2-furoyl) piperazine monohydrochloride
	Mol Mass (g/mol)	419.37
	pKa	6.5
	Solubility	61.9 mg/l
	Melting Point	270-280 °C
	Boiling Point	638.4 °C
	Appearance	White to Tan Powder

Table 2. PRH degradation with kinetics for different processes at 0.5 bar pressure drop

Processes	PRH Degradation (%)	TOC Reduction (%)	k × 10³
Only Aeration	0	0	0
Only H ₂ O ₂	10	7	1.8
Only pH 4	< 2	0	0.3
Conventional Al- Vortex Diode			
Only HC	31	15	6.2
HC+ Aeration	39	26	8.2
HC + (1:100) H ₂ O ₂	96	32	53.6
HC + (1:200) H ₂ O ₂	100	34	460.5
HC + (1:500) H ₂ O ₂	100	24	460.5
HC + pH 4	100	35	115.1
HC + pH 9	0.5	1	0.01
Dual activity Cu- vortex diode			
Only HC	35	30	7.2
HC+ Aeration	46	35	10.3
HC + (1:100) H ₂ O ₂	97	37	58.4
HC + (1:200) H ₂ O ₂	100	55	921
HC + (1:500) H ₂ O ₂	100	30	460.5
HC + pH 4	100	41	921
HC + pH 9	5	2	0.8

References:

1. V.V. Ranade, ACS Engineering Au, 2, 461, 2022.
2. T. A. Bimestre, J. A. M. Júnior, E. V. Canettieri, C. E. Tuna, Bioresour Bioprocess, 9,7, 2022.
3. N. Asaithambi, P. Singha, M. Dwivedi, S. K. Singh, J Food Process Eng, 42, e13144, 2019.
4. S. S. Arya, P. R. More, M. R. Ladole, K. Pegu, A. B. Pandit, Ultrason Sonochem, 98, 106504, 2023.
5. K. K. Jyoti, A.B. Pandit, Ultrason Sonochem, 10, 255, 2003.
6. M.B. Mane, V. M. Bhandari, K. Balapure, V. V. Ranade, Ultrason Sonochem, 61, 105272, 2020.
7. M.B. Mane, V. M. Bhandari, V. V. Ranade, J. Water Proc.engineering, 43, 102280, 2021.
8. N. B. Suryawanshi, V. M. Bhandari, L. G. Sorokhaibam, V. V. Ranade, Sci Rep, 6, 33021, 2016.
9. D. Dixit, P. Thanekar, V. M. Bhandari, Chem. Eng. Process.: Process Intensif., 172, 108799, 2022.
10. P. Thanekar, P. Gogate, Fluids, 3, 98, 2018.
11. A. V. Mohod, P.H. Palharim, B. Ramos, P. F. Moreira, A. C. S. C. Teixeira, R. Giudici, Environ. Qual. Manag., 33, 377, 2023.
12. M. V. Bagal, V. Rajan, S. Shinde, V. Gole, B. V. Banerjee, Adv. Environ. Technol., 10, 55, 2024
13. V.V. Ranade, V. M. Bhandari, S. Nagarajan, P. V. Sarvothaman, A. T. Simpson, Wiley, 2022.
14. V. V. Ranade, and V.M. Bhandari, Industrial Wastewater Treatment, Recycling and Reuse, Elsevier, 06975, 2014.
15. D. Dixit, P. Thanekar, V. M. Bhandari, Chem. Eng. Res. Des., 192, 310, 2023.
16. D. Dixit, P. Thanekar, V. M. Bhandari, Chem. Eng. Res. Des., 199, 238, 2023.
17. J. Basiri Parsa, S. A. Ebrahimzadeh Zonouzian, Ultrason Sonochem, 20, 1442, 2013
18. T. Ben-Moshe, I. Dror, B. Berkowitz, Appl Catal B, 85, 207-211, 2009.
19. S. Wang, S. Gao, J. Tian, Q. Wang, T. Wang, X. Hao, F. Cui, J Hazard Mater, 387, 121995, 2020.
20. C. Li, N. de Melo Costa Serge, R. F. P. Nogueira, S. Chiron, V. Goetz, Environ. Sci. Pollut. Res. Int., 29, 71709, 2022.

21. D. Dixit, P. Thanekar, V. M. Bhandari, *Chem. Eng. Process.: Process Intensif.*, 193, 109572, 2023.
22. V. Naddeo, V. Belgiorno, D. Kassinos, D. Mantzavinos, S. Meric, *Ultrason Sonochem*, 17, 179, 2010.
23. Al-Qaim, F. F., *Malaysian Journal of Analytical Science*, 20, 726, 2016.
24. F. F. Al-Qaim, M. P. Abdullah, M. R. Othman, Z. H. Mussa, Z. Zakaria, J. Latip, W. M. Afiq, *J. Braz. Chem. Soc.*, 26, 1124, 2015.
25. F. F. Al-Qaim, Z. H. Mussa, A. Yuzir, J. Latip, M. R. Othman, *J. Environ. Sci.*, 74, 134, 2018.
26. Z. H. Mussa, F. F. Al-Qaim, Z. H. Al-Qaim, J. Latip, 68, 811, 2021.
27. Y. M. Mat Zaini, L. Dina Amalia Purba, N. Abdullah, A. Yuzir, K. Iwamoto, S. E. Mohamad, *Mater Today Proc*, 65, 3007, 2022.
28. N. F. Mohd Mohsi, A. Apandi, M. J. Megat Mohd Noor, F. N. MD Akhir, N. Sugiura, M. Utsumi, N. Othman, Z. Zakaria, H. Hara, *J Gen Appl Microbiol*, 66, 8, 2020.
29. L. Kumar, R. Jog, S. Singh, A. Bansal, *AAPS Pharm SciTech*, 14, 757, 2013.
30. M. Bakshi, T. Ojha, S. Singh, *J Pharm Biomed Anal*, 34, 19, 2004.
31. S. Raut-Jadhav, D. Saini, S. Sonawane, A. Pandit, *Ultrason Sonochem*, 28, 283, 2016.
32. S. Raut-Jadhav, V. K. Saharan, D. Pinjari, S. Sonawane, D. Saini, A. Pandit, *J Hazard Mater*, 261, 139, 2013.
33. A. Bokhari, J. J. Klemeš, S. Asif, *Chem Eng Trans*, 88, 949, 2021.
34. P. B. Patil, P. Thanekar, V. M. Bhandari, *Ind Eng Chem Res*, 62, 1926, 2023.
35. P. B. Patil, P. Thanekar, V. M. Bhandari, *Chem. Eng. Res. Des.*, 187, 623, 2022.
36. P. B. Patil, V. M. Bhandari, V. V. Ranade, *Chem. Eng. Process.: Process Intensif.*, 166, 108485, 2021.
37. P. Thanekar, M. Panda, P. R. Gogate, *Ultrason Sonochem*, 40, 567, 2018.
38. P. K. Mishra, P. R. Gogate, *Sep Purif Technol*, 75, 385, 2010.
39. V. K. Saharan, M. A. Rizwani, A. A. Malani, A. B. Pandit, *Ultrason Sonochem*, 20, 345, 2013.

Raman Spectroscopy in the Research of Carbon Materials

Kinshuk Dasgupta

Materials Group, Bhabha Atomic Research Centre, Mumbai 400085

Email: kdg@barc.gov.in

Received: 13.8.2024, Revised: 3.1.2025, 24.1.2025, Accepted: 25.1.2025

Abstract:

Raman spectroscopy has become an indispensable tool in the field of material science, especially in the study of carbon materials. Its non-destructive nature, sensitivity to molecular vibrations, and ability to provide detailed information about the chemical composition, structure, and crystallinity make it a powerful technique for characterizing a wide range of carbon-based materials. This article delves into the significance of Raman spectroscopy in the research of carbon materials, exploring its principles, the types of carbon materials it can analyze, and the key findings it has facilitated.

Keywords: Raman spectroscopy; Carbon materials; Enhanced Raman techniques; Radial breathing mode; Stokes and anti-Stokes scattering

1. Introduction:

Raman spectroscopy is a vibrational spectroscopic technique based on the inelastic scattering of monochromatic light, usually from a laser source. When light interacts with a material, most photons are elastically scattered (Rayleigh scattering), but a small fraction undergoes inelastic scattering (Raman scattering). This inelastic scattering results in a shift in the energy of the scattered photons, corresponding to the vibrational energies of the molecules in the sample. The Raman spectrum, which plots intensity versus the Raman shift (measured in wavenumbers, cm^{-1}), provides a fingerprint of the material's molecular vibrations.

1.1 Principles of Raman Spectroscopy

Raman spectroscopy relies on the Raman Effect, first observed by C.V. Raman in 1928¹. When a photon interacts with a molecule, it can either gain or lose energy, depending on the vibrational state of the molecule. This energy difference between the incident and scattered photons gives rise to the Raman shift. The Raman spectrum thus provides information about the vibrational modes of the molecules in the sample.

The key features of a Raman spectrum include²:

Raman Shift ($\Delta\nu$): The difference in wavenumber between the incident and scattered light, typically measured in cm^{-1} .

Intensity: The strength of the Raman signal, which depends on factors such as the concentration of the molecules and the polarizability of the bonds.

Peak Position: The specific wavenumber at which a peak occurs, corresponding to a particular vibrational mode of the molecule.

Peak Width: The broadness of the peak, which can indicate the degree of crystallinity or disorder in the material.

1.2 Theory of Raman Scattering

Raman scattering is an inelastic light scattering phenomenon where the frequency of the scattered light differs from that of the incident light. This frequency shift arises from the interaction of the incident light with molecular vibrations within the sample. When a photon interacts with a molecule, it can either excite a vibrational mode (Stokes scattering) or de-excite an already excited mode (anti-Stokes scattering). Stokes scattering results in a lower-frequency scattered photon, while anti-Stokes scattering produces a higher-frequency photon. The intensity ratio of Stokes and anti-Stokes lines provides valuable information about the vibrational energy levels and temperature of the sample³. The schematic of the energy transition is given in **Fig. 1**.

1.3 Working of Raman Spectrometer

A monochromatic light source, usually in the visible or near-infrared region, provides the excitation energy for Raman scattering. The choice of laser wavelength depends on the sample and the desired information. The material to be analysed is placed in the path of the laser beam. Collection optics focus the scattered light from the sample onto the entrance slit of the spectrometer. A filter, such as a notch filter or edge filter, removes the intense Rayleigh scattering from the Raman signal, which is crucial because Raman scattering is typically very weak compared to Rayleigh scattering. The monochromator disperses the Raman scattered light into its constituent wavelengths, typically consisting of a diffraction grating that diffracts the light based on its wavelength, separating the different Raman shifts. A sensitive detector, such as a charge-coupled device (CCD) array detector, records the intensity of the Raman scattered light at each wavelength. The schematic of the Raman spectrometer is given in **Fig.2**.

2. Carbon Materials and Their Importance

Carbon materials, owing to their unique properties, have become central to various fields, including electronics, energy storage, and nanotechnology. These materials exist in several allotropes, including graphite, diamond, graphene, carbon nanotubes, and fullerenes, each with distinct structures and properties ⁴.

Graphite: Composed of layers of hexagonally arranged sp^2 hybridized carbon atoms in ABAB.....stacking (**Fig. 3a**), graphite is used in a wide range of applications, from lubricants to electrodes.

Diamond: Known for its hardness and thermal conductivity, diamond is sp^3 hybridized FCC structure (**Fig. 3b**) used in cutting tools, optics, and electronics.

Graphene: A single layer of sp^2 hybridized carbon atoms arranged in a hexagonal lattice (**Fig. 3c**), graphene exhibits exceptional electrical, thermal, and mechanical properties.

Carbon Nanotubes (CNTs): Cylindrical nanostructures with sp^2 hybridized carbon atoms (**Fig. 3d**) having remarkable strength, electrical conductivity, and thermal stability.

Fullerenes: Spherical or cage like structure (**Fig. 3e**) composed entirely of carbon, with potential applications in medicine, electronics, and materials science.

3. Raman Spectroscopy in Carbon Materials

Raman spectroscopy is particularly well-suited for studying carbon materials due to its ability to probe the vibrational modes associated with the sp^2 and sp^3 hybridized carbon atoms. The technique can provide detailed insights into the structure, defects, electronic properties, and interactions of carbon materials.

3.1 Raman Spectroscopy of Graphite and Graphene

Graphite and graphene are among the most studied carbon materials using Raman spectroscopy. The graphene used in this study has been synthesised in-house by CVD method⁵. The graphite were obtained from Tianjin Dingshengxin Chemical Industry Co. Ltd. The Raman spectra were acquired using a 514 nm diode laser with an acquisition time of 1 second and a power of 20 mW. These parameters were consistently used for obtaining the spectra of other carbon nanomaterials analyzed in this study. Few mg of sample was spread on a glass slide and spectrum was acquired. The Raman spectrum (refer **Fig. 4**) of these materials is characterized by several key features ⁶:

G Band: The G band, observed around 1580 cm^{-1} , corresponds to the in-plane vibrational mode (E_{2g}) of sp^2 carbon atoms. It is present in all sp^2 carbon systems and is a signature of graphitic materials.

D Band: The D band, appearing around 1350 cm^{-1} , is associated with the presence of defects or disorder in the sp^2 carbon lattice. It arises due to the breathing modes of sp^2 rings and is activated by defects such as edges or vacancies in the lattice. The intensity ratio of the D to G band (I_D/I_G) is often used as a measure of the degree of disorder in the material.

2D Band: The 2D band, also known as the G' band, is a second-order overtone of the D band, observed around 2700 cm^{-1} . In graphene, the 2D band is particularly important as it provides information about the number of layers and the stacking order of the graphene sheets. In single-layer graphene, the 2D band is a sharp, single peak, whereas in multi-layer graphene, it splits into multiple components.

D' Band: The D' band, appearing around 1620 cm^{-1} , is another defect-related peak, often observed in conjunction with the D band. The intensity of the D' band, along with the D and G bands, can provide insights into the nature and concentration of defects in the material.

D'' Band: The D'' mode is a higher-order overtone or combination. It typically appears at higher wavenumbers compared to the D band and is indicative of more complex vibrational interactions within the material. The presence and intensity of the D'' band can provide insights into the material's structural properties and defect levels.

D+D'' Peak: The D+D'' peak is observed around 2425 cm^{-1} , results from simultaneous interactions involving both the D and D'' phonons. This peak is particularly intense in disordered graphene materials and serves as an indicator of the material's quality and structural characteristics.

In graphite with small defect concentration additional peaks like D+D' also appear.

Raman spectroscopy has been instrumental in characterizing graphene's properties, such as layer number, quality, and the effects of strain or doping. For instance, the 2D band analysis allows researchers to distinguish between single-layer and multi-layer graphene, while the D band intensity reveals information about defects or functionalization.

3.2 Raman Spectroscopy of Carbon Nanotubes

Carbon nanotubes (CNTs) exhibit a rich and complex Raman spectra, reflecting their unique structures and electronic properties. Single-walled CNT (SWCNT) and multi-walled CNT (MWCNT) show different features⁷. CNTs used in this study were synthesized in-house by FC-CVD method⁸⁻¹⁰.

Single-walled carbon nanotubes (SWCNTs) are one of the most fascinating nanomaterials, renowned for their unique structural, electrical, and mechanical properties. Raman spectroscopy plays a critical role in characterizing these properties, providing insights into the diameter, chirality, electronic structure, and defect density of SWCNTs. The Raman spectrum of SWCNTs is rich with information and can be analyzed by focusing on several key features: the radial breathing mode (RBM), the G-band, the D-band, and the 2D-band ¹¹.

Radial Breathing Mode (RBM): The radial breathing mode (RBM) is one of the most characteristic and important features in the Raman spectrum of SWCNTs. It is a low-frequency mode, typically observed in the range of 100-300 cm⁻¹, and corresponds to the coherent radial expansion and contraction of the nanotube. The frequency of the RBM (ω_{RBM}) is inversely proportional to the nanotube diameter (d), and can be expressed approximately by the following empirical relation ¹²:

$$\omega_{\text{RBM}} = C_1/d + C_2$$

where C_1 and C_2 are constants that depend on the environment and nanotube characteristics. This mode is particularly useful because it allows researchers to determine the diameter of the SWCNTs directly from the Raman spectrum. **Fig. 5 (a-d)** shows how after capturing RBM mode from different positions of a SWCNT bundle we can get diameter distribution.

The RBM is sensitive to the environment surrounding the nanotubes. For example, if the nanotube is in a bundle or interacting with a substrate, the RBM frequency may shift. Additionally, the intensity of the RBM is linked to the resonance condition between the incident laser energy and the electronic transition energy of the SWCNT, which provides information on the electronic structure of the nanotube.

G-Band: The G-band is another critical feature in the Raman spectrum of SWCNTs. It is typically observed around 1580 cm⁻¹ and arises from the in-plane stretching vibrations of carbon-carbon bonds in the sp² hybridized carbon atoms. Unlike graphene or graphite, where the G-band appears as a single peak, the G-band in SWCNTs is split into two components: G+ and G- (**Fig. 6**).

The G+ band corresponds to the longitudinal optical (LO) phonon mode, which involves vibrations along the axis of the nanotube. It is usually located at a higher frequency (~1590 cm⁻¹) and is relatively sharp.

The G- band corresponds to the transverse optical (TO) phonon mode, which involves vibrations perpendicular to the nanotube axis. It appears at a lower frequency ($\sim 1560\text{-}1570\text{ cm}^{-1}$) and is broader than the G+ band.

The splitting of the G-band is particularly important because it can be used to distinguish between metallic and semiconducting SWCNTs. In semiconducting SWCNTs, the G- band is narrow and well-defined, while in metallic SWCNTs, it is broader and lower in frequency. This difference is due to the electron-phonon coupling, which is stronger in metallic nanotubes.

The study of anti-Stokes Raman spectra of single-walled carbon nanotubes reveals significant asymmetries compared to Stokes spectra, attributed to unique resonant enhancement phenomena influenced by their one-dimensional electronic density of states, which allows for selective identification of different nanotube types under specific laser excitation conditions¹³.

D-Band: The D-band, typically observed around 1350 cm^{-1} , is associated with the presence of defects or disorder in the SWCNT structure. It arises from the breathing modes of sp^2 carbon atoms in rings and is activated by the presence of defects, such as vacancies, impurities, or functional groups that break the symmetry of the carbon lattice.

The intensity ratio of the D-band to the G-band (I_D/I_G) is often used as a measure of the defect density in SWCNTs. A higher I_D/I_G ratio indicates a greater degree of disorder or a higher concentration of defects. This ratio is particularly useful for evaluating the quality of SWCNTs, especially after processes like functionalization or chemical treatment.

2D-Band (G'-Band): The 2D-band, also known as the G'-band, is a second-order overtone of the D-band and is typically observed around $2600\text{-}2700\text{ cm}^{-1}$. Unlike the D-band, the 2D-band does not require the presence of defects for activation and is always present in the Raman spectrum of SWCNTs.

The 2D-band provides additional information about the electronic structure of the SWCNTs. Its shape, position, and intensity can vary depending on the number of layers, the presence of strain, and the electronic properties of the nanotubes. In SWCNTs, the 2D-band is usually sharp and symmetric, and its intensity is strongly dependent on the resonance condition with the incident laser energy.

Multi-walled carbon nanotubes (MWCNTs) consist of multiple concentric single-walled carbon nanotubes (SWCNTs), with each layer having a different diameter and possibly different chirality. The Raman spectrum of MWCNTs shares many features with that of SWCNTs, but the additional layers and the complex interactions between them lead to some

distinct characteristics. The RBM peak in MWCNT is generally missing and the splitting of the G band in MWCNT is not witnessed in MWCNT unlike SWCNT as the combined effect of multiple tubes in the MWCNT nullifies the effect (**Fig. 7**). The Raman spectrum of double-walled carbon nanotubes (DWCNT) is characterized by distinct peaks such as the radial breathing mode (RBM), D band, and G band, where the RBM frequency is sensitive to the inner and outer tube diameters; in contrast, multi-walled carbon nanotubes (MWCNT) typically show broader peaks and a more complex spectral profile due to multiple concentric layers, leading to overlapping signals that complicate the interpretation of individual modes ¹⁴

3.3 Raman Spectroscopy of Diamond

Diamond, with its purely sp^3 carbon bonding, exhibits a characteristic Raman peak at 1332 cm^{-1} , corresponding to the stretching of the carbon-carbon bonds in the diamond lattice. Diamond used in this study is diamond powder used in polishing industry ¹⁵. The sharpness and position of this peak are indicative of the diamond's purity and crystallinity. Raman spectroscopy is widely used to assess the quality of synthetic diamonds, identify defects, and study phase transitions, such as the conversion of diamond to graphite under high temperatures or pressures¹⁶.

In addition to pure diamond, Raman spectroscopy is also employed to study diamond-like carbon (DLC) films (**Fig. 8**), which are amorphous carbon materials with a mixture of sp^2 and sp^3 bonding. The Raman spectrum of DLC typically shows broad peaks around 1350 cm^{-1} (D band) and 1550 cm^{-1} (G band), similar to those of disordered graphite, but with differences in peak position and intensity that reflect the sp^2/sp^3 ratio and the degree of disorder.

3.4 Raman Spectroscopy of Fullerenes

Fullerenes, such as C₆₀ and C₇₀, are spherical carbon molecules with unique electronic and vibrational properties ¹⁷. The Raman spectra of fullerenes are characterized by several distinct peaks corresponding to the vibrational modes of the carbon atoms in the cage structure. For example, the Ag(2) mode of C₆₀, observed around 1469 cm^{-1} , is a prominent feature in its Raman spectrum (**Fig. 9**).

Raman spectroscopy has been crucial in studying the structural and electronic properties of fullerenes, as well as their interactions with other materials. For instance, the shifts in Raman peaks can provide information about the charge transfer between fullerenes and dopant molecules, which is important in understanding their behaviour in organic photovoltaics and other electronic applications.

3.5 Effect of Excitation Wavelength

The intensity of Raman scattering is inversely proportional to the fourth power of the laser wavelength. This means that longer wavelengths (e.g., near-infrared) produce weaker Raman signals compared to shorter wavelengths (e.g., UV or visible light). For instance, using a near-infrared laser can result in spectra that are up to 15 times less intense than those obtained with a UV laser under identical conditions.

Resonance Enhancement: The choice of laser wavelength can also affect resonance conditions, which enhance specific spectral features. For example, certain phonon populations in carbon materials may resonate differently depending on the excitation wavelength, leading to shifts in the D band frequency. This resonance effect is crucial for accurately interpreting the microstructure of materials like graphite and carbon nanotubes.

4. Enhanced Raman Spectroscopic Techniques

4.1 Surface-enhanced Raman Spectroscopy

Surface-enhanced Raman spectroscopy (SERS) is a powerful analytical technique used to enhance the Raman signals of carbon materials by leveraging plasmonic effects from metallic nanostructures, such as silver or gold nanoparticles¹⁸. This method is particularly effective for detecting low-concentration analytes, revealing subtle structural features, and identifying functional groups in carbon-based materials. SERS enables high sensitivity and specificity, making it an invaluable tool for studying carbon nanomaterials, such as graphene, carbon nanotubes, and amorphous carbon, in various applications ranging from sensing to catalysis.

4.2 Tip-enhanced Raman Spectroscopy

Another area of ongoing research is the development of tip-enhanced Raman spectroscopy (TERS), which combines the spatial resolution of atomic force microscopy (AFM) with the chemical sensitivity of Raman spectroscopy¹⁹. It utilizes a sharp metallic tip, often coated with a noble metal like gold or silver, to enhance the Raman signal from molecules located at the tip apex. TERS has the potential to provide nanoscale insights into carbon materials, enabling the study of local variations in structure and composition that are not accessible with conventional Raman spectroscopy.

TERS allows for highly localized Raman scattering measurements on carbon materials. By using a sharp metal tip to concentrate the incident laser light, TERS provides nanoscale spatial resolution, enabling the characterization of individual carbon nanotubes, graphene layers, and

defects within these materials²⁰. This technique has proven valuable in understanding the structure, properties, and electronic behavior of carbon-based nanomaterials.

5. Applications of Raman Spectroscopy in Carbon Material Research

Raman spectroscopy has been applied to a wide range of studies involving carbon materials, contributing to advancements in various fields. Some of the key applications include:

5.1 Characterization of Graphene-Based Materials: Raman spectroscopy is widely used to characterize graphene and its derivatives, such as graphene oxide (GO) and reduced graphene oxide (rGO). The technique provides insights into the number of layers, degree of oxidation, and reduction efficiency, which are critical for tailoring the properties of graphene-based materials for specific applications. To determine the number of layers in graphene oxide using Raman spectroscopy, one can analyze the intensity ratio of the 2D band to the G band (I_{2D}/I_G), as well as observe the peak positions and shapes, where a higher ratio typically indicates fewer layers and a broader 2D peak suggests an increase in layer number²¹. The correlation between the full width at half maximum (FWHM) of the Raman 2D peak and the number of graphene layers indicates that as the number of layers increases, the FWHM generally decreases, with single-layer graphene exhibiting a FWHM of approximately 28.7 cm^{-1} and multilayer graphene showing broader peaks due to interlayer interactions and disorder²². Raman spectroscopy is a powerful tool for differentiating between GO and reduced rGO by analyzing the intensity ratios and positions of specific peaks, particularly the D, G, and D' bands; for instance, the energy difference between the D' and G peaks can quantitatively define the degree of reduction, where a negative difference indicates GO, a small positive difference indicates rGO, and a larger positive difference indicates pristine graphene²³.

5.2 Quality Control of Carbon Nanotubes: The synthesis of high-quality CNTs is challenging, and Raman spectroscopy serves as a valuable tool for quality control. By analyzing the RBM, G, and D bands, researchers can assess the purity, diameter distribution, and defect density of CNTs, ensuring their suitability for applications in electronics, composites, and energy storage. To quantify the amorphous content in carbon nanotubes (CNTs) using Raman spectroscopy, one can analyze the intensity ratios of the D-band and G-band, specifically the I_D/I_G ratio, where a higher ratio indicates a greater presence of amorphous carbon due to increased disorder in the structure. This method effectively distinguishes between crystalline and amorphous phases in carbon materials²⁴.

5.3 Studying Defects and Functionalization: Defects and functional groups play a crucial role in determining the properties of carbon materials. Raman spectroscopy is highly sensitive to these features, making it an ideal technique for studying the effects of defects, doping, and functionalization on the material's properties. For example, in graphene, the I_D/I_G ratio provides a measure of the defect density, while in CNTs, the appearance of new peaks in the Raman spectrum can indicate successful functionalization.

5.4 In-Situ and Operando Studies: Raman spectroscopy can be performed in-situ, allowing researchers to monitor changes in carbon materials under various conditions, such as temperature, pressure, or chemical environment. This capability is particularly useful for studying the behaviour of carbon materials in real-time, such as during the electrochemical cycling of batteries or the growth of graphene by chemical vapour deposition (CVD).

5.5 Nanotechnology and Device Fabrication: Raman spectroscopy is employed in the fabrication and characterization of carbon-based nanodevices, such as graphene transistors and CNT-based sensors. The technique provides valuable information about the structural and electronic properties of the materials, enabling the optimization of device performance.

6. Challenges and Future Directions

While Raman spectroscopy has proven to be an invaluable tool in carbon material research, it is not without its challenges. One of the primary challenges is the interpretation of complex spectra, especially in materials with a high degree of disorder or in heterogeneous systems. Advanced data analysis techniques, such as multivariate analysis and machine learning, are being developed to address these challenges and extract more detailed information from Raman spectra.

7. Conclusions

Raman spectroscopy has become an essential technique in the research of carbon materials, providing detailed insights into their structure, properties, and behaviour. From the characterization of graphene and CNTs to the study of diamond and fullerenes, Raman spectroscopy has played a pivotal role in advancing our understanding of carbon-based materials and enabling their applications in various fields. As the field of material science

continues to evolve, Raman spectroscopy will undoubtedly remain a key tool for exploring the fascinating world of carbon materials, driving innovation and discovery in the years to come.

Acknowledgement:

I thank Shri Rajath Alexander and Shri Subham Kumar for helping in drafting the manuscript. I extend my gratitude to Dr. Jyoti Prakash, Shri Rajath Alexander, Shri Amit Kaushal and Shri P.T. Rao for generating data on carbon materials.

Figures:

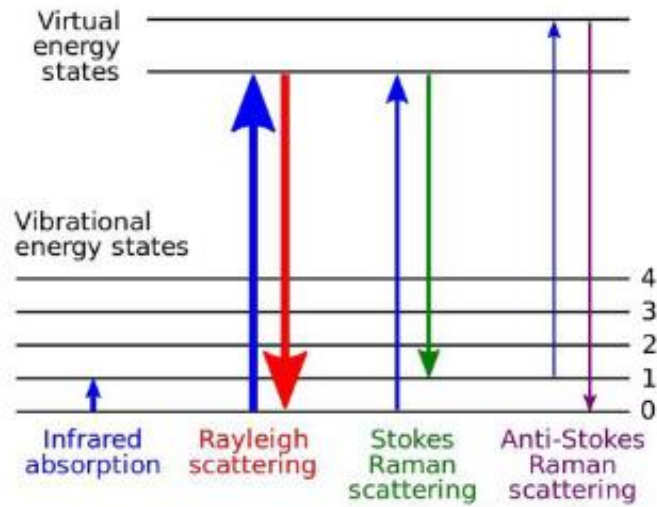


Fig. 1: Energy transition in Rayleigh, Stokes, anti-Stokes scattering ²⁵

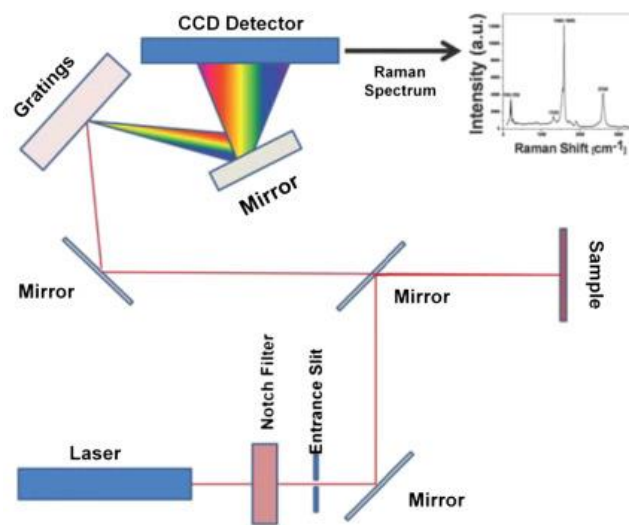


Fig. 2: Schematic of Raman spectrometer ²⁶

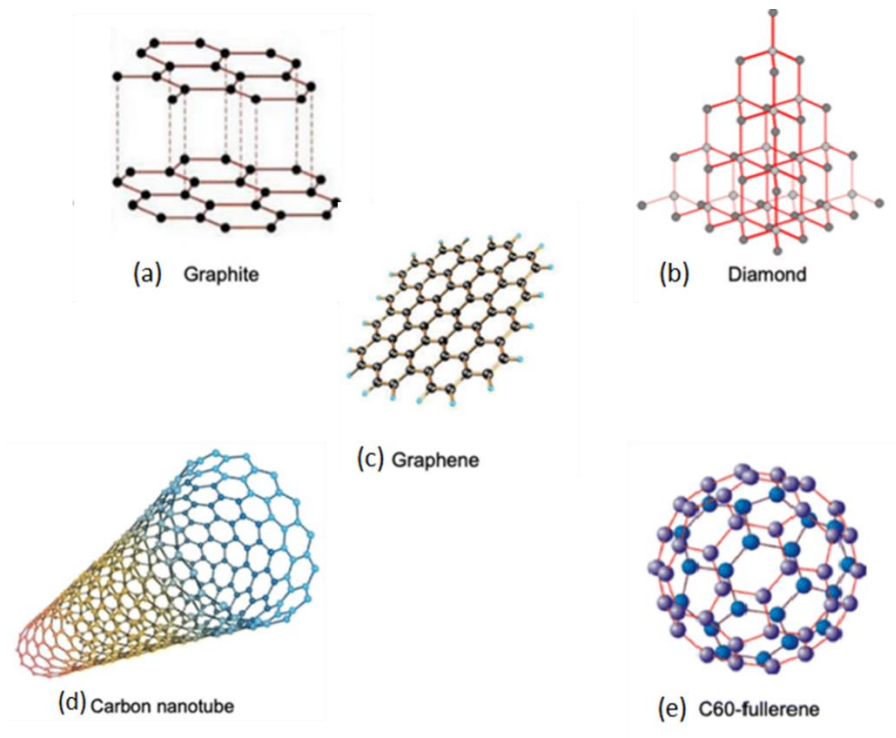


Fig. 3 (a-e): Different structure of carbon ²⁷

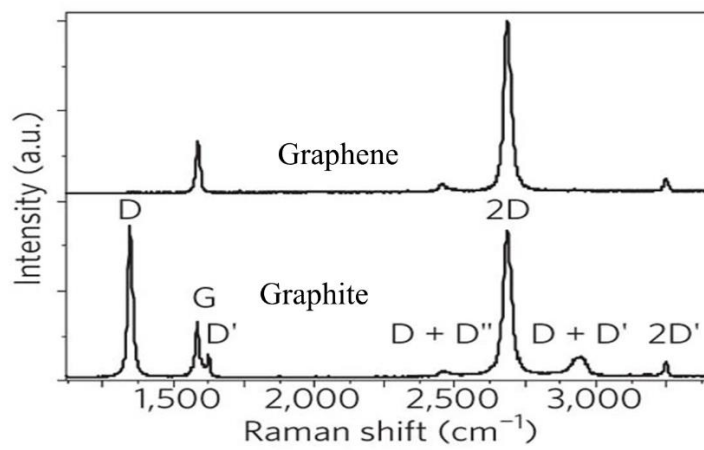


Fig. 4: Raman spectra of graphene and graphite ²⁸

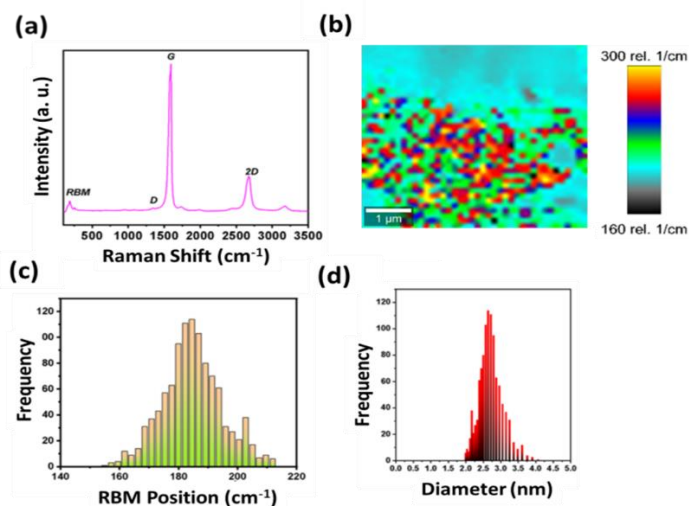


Fig. 5: (a) Raman spectra of SWCNT, (b) RBM peak mapping in SWCNT in SWCNT bundle, (c) distribution of RBM peak position, and (d) diameter distribution of SWCNT determined from RBM position ¹¹

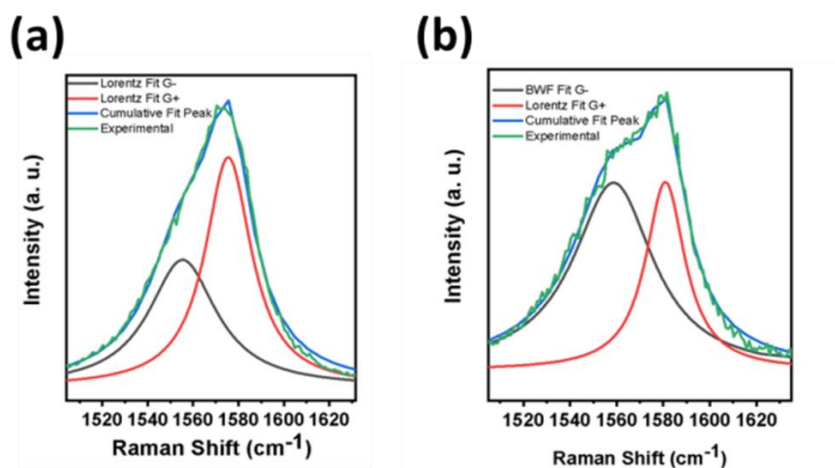


Fig. 6: (a) Deconvolution of G band of metallic SWCNT, and (b) deconvolution of G band of semiconductor SWCNT ¹¹

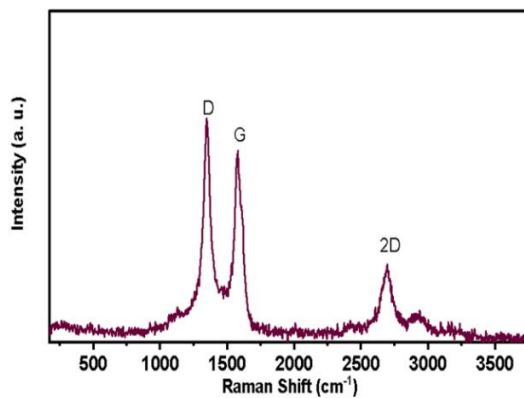


Fig. 7: Raman spectrum of MWCNT ¹¹

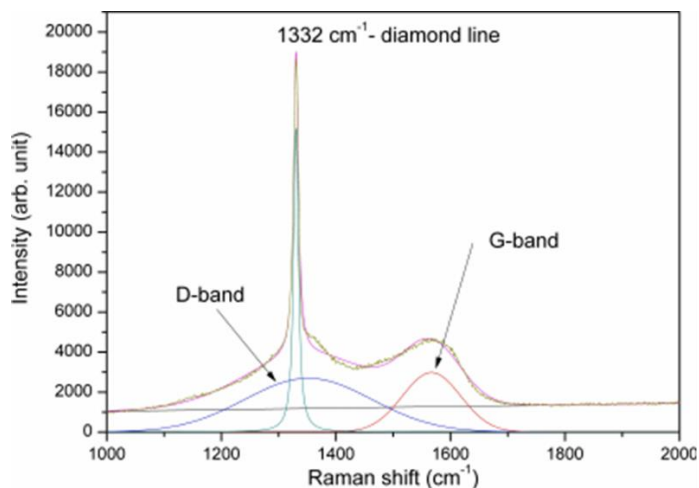


Fig. 8: Raman spectrum from diamond and DLC ²⁹

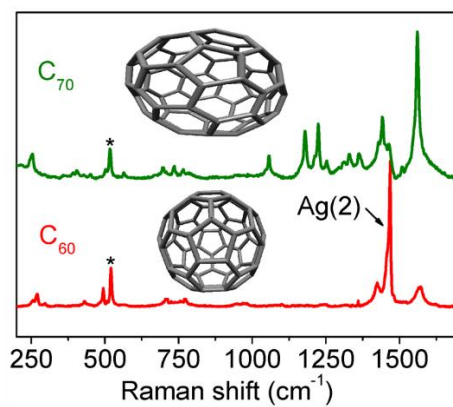


Fig. 9. Raman spectra from C60 and C70 fullerenes

References:

1. C. V. Raman, Indian Journal of physics 2, 387,1928.
2. D. Long, Chichester and New York: Wiley, 2002.
3. B. Schrader, Infrared and Raman spectroscopy: methods and applications, John Wiley & Sons, 2008.
4. K. Dasgupta and D. Sathiyamoorthy, Materials science and technology, 19, 995,2003
5. M. D. Yadav, K. Dasgupta, A. Kushwaha, A. P. Srivastava, A. W. Patwardhan, D. Srivastava and J. B. Joshi, Materials Letters, 199, 180, 2017.
6. A. C. Ferrari, Solid state communications, 143, 47, 2007.
7. M. S. Dresselhaus, A. Jorio, M. Hofmann, G. Dresselhaus and R. Saito, Nano Letters, 10, 751 2010,
8. A. Kaushal, R. Alexander, M. Joshi, J. Singh and K. Dasgupta, Chemical Engineering Journal, 484, 149254, 2024.
9. R. Alexander, A. Kaushal, S. Acharya, J. Prakash, J. Bahadur and K. Dasgupta, Chemical Engineering Journal, 503, 158460, 2025.
10. R. Alexander, A. Khausal, J. Bahadur and K. Dasgupta, Carbon Trends, 9, 100211, 2022.
11. R. Alexander, J. Prakash, A. Kaushal and K. Dasgupta, Phys News, 50, 28. 2020.
12. P. T. Araujo, I. O. Maciel, P. B. C. Pesce, M. A. Pimenta, S. K. Doorn, H. Qian, A. Hartschuh, M. Steiner, L. Grigorian, K. Hata and A. Jorio, Physical Review B, 77, 241403, 2008.
13. S. D. M. Brown, P. Corio, A. Marucci, M. S. Dresselhaus, M. A. Pimenta and K. Kneipp, Physical Review B, 61, R5137, 2000.
14. A. Jorio and R. Saito, Journal of Applied Physics, 129, 021102, 2021.
15. R. Alexander, K. V. Ravikanth, M. R. Gonal, A. P. Srivastava and K. Dasgupta, SN Applied Sciences, 2, 835, 2020.
16. S. Praver and R. J. Nemanich, Philosophical Transactions of the Royal Society of London. Series A: Mathematical, Physical and Engineering Sciences, 362, 2537, 2004.
17. M. Dresselhaus and P. Eklund, Advances in physics, 49, 705, 2000.
18. E. Le Ru and P. Etchegoin, Principles of Surface-Enhanced Raman Spectroscopy: and related plasmonic effects, Elsevier, 2008.

19. B. Pettinger, P. Schambach, C. J. Villagómez and N. Scott, Annual review of physical chemistry, 63, 379, 2012.
20. G. G. Hoffmann, M. Ghislandia and G. de Witha, Nanotechnology, 18, 315502, 2007.
21. V. Kumar, A. Kumar, D.-J. Lee and S.-S. Park, Materials, 14, 4590, 2021.
22. Z. Lin, X. Ye, J. Han, Q. Chen, P. Fan, H. Zhang, D. Xie, H. Zhu and M. Zhong, Scientific Reports, 5, 11662, 2015.
23. A. A. K. King, B. R. Davies, N. Noorbehesht, P. Newman, T. L. Church, A. T. Harris, J. M. Razal and A. I. Minett, Scientific Reports, 6, 19491, 2016.
24. S. I. Moseenkov, V. L. Kuznetsov, N. A. Zolotarev, B. A. Kolesov, I. P. Prosvirin, A. V. Ishchenko and A. V. Zavorin, Materials, 16, 1112, 2023.
25. T. Subramaniam and R. Premanand, J Laser Opt Photonics, 5, 1000189, 2018.
26. N. John and S. George, in Spectroscopic Methods for Nanomaterials Characterization, eds. S. Thomas, R. Thomas, A. K. Zachariah and R. K. Mishra, Elsevier, pp. 95-127, 2017.
27. A. Aligayev, F. Raziq, U. Jabbarli, N. Rzayev and L. Qiao, in Graphene, Nanotubes and Quantum Dots-Based Nanotechnology, ed. Y. Al-Douri, Woodhead Publishing, pp. 355-420, 2022.
28. A. C. Ferrari and D. M. Basko, Nature Nanotechnology, 8, 235, 2013.
29. A. Dychalska, P. Popielarski, W. Franków, K. Fabisiak, K. Paprocki and M. Szybowicz, Materials Science-Poland, 33, 799, 2015.

Facile Synthesis, Characterization and Photocatalytic activity of MOF-5

Manisha A. Bora^{1*}, Suhani Patel¹, Parag Adhyapak²

¹ Department of Chemistry, BJS'S ASC College, Nagar Road, Wagholi, Pune-412207

² Centre for Materials for Electronics Technology (C-MET) Panchawati, off Pashan Road, Pune-411008

*Email- bmanishabora@gmail.com,

Received: 5.1.2025, Revised: 6.1.2025, 19.1.2025, 22.1.2025 Accepted: 25.1.2025

Abstract:

Metal–Organic-Frameworks (MOFs) are highly tunable to design and functionalize, hence they are recognized as materials of interest in applied sciences. MOF-5 having formula ($Zn_4O_{13}-(C_8H_4)_3$), is a well-known MOF due to its distinctive porosity and thermal stability. MOF-5 has a 3D structure comprising of terephthalic acid and Zn_4O clusters. In the present study, the MOF-5 was synthesized using facile, ecofriendly one pot hydrothermal process at low temperature. The MOF-5 was characterized to assess intrinsic properties such as crystallinity, morphology, functional groups at surface sites, using techniques like UVDRS, FTIR, XRD and FESEM. The synthesized material was also verified for its photocatalytic activity towards dye degradation of methyl orange (MO). The synthesized material of MOF-5 displays excellent MO dye deprivation efficiency in a natural sunlight by facilitated photodegradation route.

Keywords: porous material, MOF-5, dye degradation, methyl orange (MO)

1. Introduction:

In recent times, the field of Metal Organic Frameworks (MOFs) has become one of the foremost survey stresses in assorted fields of investigation. MOF is a coordination complex with organic ligands comprising prospective cavities. MOF-5 comprises of tetrahedral $[Zn_4O]^{6+}$ masses associated by benzene dicarboxylic acid linkers (BDC) to form a 3D cubic complex. These materials which are prepared by associating inorganic and organic units show pronounced flexibility with which the components geometry, size, and functionality can be varied¹⁻³. Metal-organic frameworks symbolize porous materials that are building up from

metal ions or metallic complexes and organic ligands. Organic molecules containing one or more N-donor or O-donor atoms are normally used as organic ligands to bridge between the metal ions in MOFs. Carboxylates, pyridyl and cyano compounds, oxalic acid, and benzene, phosphonates, sulfonates, and crown ethers are the most common ligands used. The anions counterbalance the positive charge of cationic MOFs and influence the supra molecular structure either being coordinated to the metal ions or by occupying the pores of the structure⁴⁻⁶. The 3D assembly of MOFs is designed due to robust coordination bonds between the metal ions and the organic ligands and displays voids and inner surfaces, which are occupied by counter ions, guest molecules, and/or solvate molecules. Other types of interactions, such as hydrogen bonds, metal-metal bonds, and π - π interactions can occur and contribute to the stability of the MOFs. The post-synthetic alteration of the MOFs later their production has been widely used to introduce functional assemblies and give the anticipated physico-chemical properties⁷⁻⁹. The possibility of functionalization of the size and shape of the pores compromises high potential for solicitations in the energy and environment, with gas sorption, storage, and separation, as well as metal ions and toxic molecules for analytical and sensing dedications, insertion of drugs, and biologically important molecules as smart transporters for anti-cancer and anti-microbial remedies. Since the novelty of these spongy porous materials, their hopeful solicitations in several fields such as, gas storage, energy storage, catalysis, dye degradation, drug synthesis, etc., remain to spread and have drawn commitment of investigators for innovative analysis and uses. High porosity gives these materials a high-class distinguishing possession¹⁰⁻¹⁴. In the present work by considering the remarkable photocatalytic possessions of Zn-based MOFs, the present work focuses on facile synthesis of MOF-5 and its application as a photocatalyst for MO dye degradation was evaluated. The photodegradation action of the prepared MOF-5 sample was inspected against methylene Orange (MO) dye in presence of natural sunlight. It is exciting to find that the alteration in morphology and elemental content has extraordinary consequence on photocatalytic activity of the MOF-5 material for dye degradation phenomenon. The current work highlights the solicitations of MOF-5 for MO degradation in sunlight.¹⁵⁻²¹

2. Experimental Section

2.1 Materials and methods

The entire chemicals castoffs for the production of MOF-5 were of AR grade. Benzene dicarboxylic acid (BDC), zinc acetate dihydrate, N, N-dimethyl formide (DMF), ethanol, methyl orange, and DI water were used for the synthesis and degradation studies obtained

from SD Fine India Ltd. All the chemicals were used as received without any additional purification.

2.2 Synthesis of MOF-5

MOF-5 was synthesized according to a modified hydrothermal method. Zinc acetate (3.83 mmol, 0.85g) and Benzene dicarboxylic acid (BDC) (5.30 mmol, 0.95g) were dissolved in 7 ml N, N-Dimethyl formide (DMF) and 3 ml ethanol (ratio of 7:3) in a conical flask with constant stirring up to 2.5 hour at room temperature. After stirring, the mixture was centrifuged for 5 min at 2000 rpm. Then it was heated hydrothermally at 80°C for 2 hrs. The reaction mixture was then cooled and filtered. The solid product obtained was then washed with DMF and dried in oven. Analytical technique namely, UV-Vis, FTIR, XRD and FESEM were used confirm the various properties of synthesized material of MOF-5.

2.3 Study of photocatalytic performance of MOF-5

In the present work, the effect of initial photo catalyst (MOF-5) concentration under direct sunlight irradiation was inspected by changing the initial concentration from 10 to 50 mg per 100 ml of 10 mg methyl orange (MO) dye solutions. After adding MOF-5 to methyl orange solution, it was exposed to ultrasonication for 1 minute to get uniform mixture. The solution mixture was agitated in the dark for 20-30 min to attain adsorption-desorption equilibrium. Then absorbance was found out in colorimeter without keeping the test-tube in the sunlight. After taking absorbance test-tube was kept in the sunlight for photodegradation of MO and absorbance was taken every day for consecutive 10 days. All the observations were noted for 0.05M, 0.1M and 0.5M concentrations of the MO. The above method was repeated to obtain the data for dye degradation under dark circumstances.

2.4 Characterization

The pure MOF-5 was characterized to investigate its intrinsic possessions using different instrumental methods. UV-visible absorption measurements were taken by a UV-VIS-NIR spectrophotometer (SHIMADZU Pharmespec UV-1700). The UV-Vis spectroscopy was carried out in the range of 200–700 nm. The functional groups of MOF-5 was recognized using Fourier transform infrared (FTIR, Perkin Elmer/Spectrum II) spectrometer using ATR disc mode in the range of 500–4000cm⁻¹ wavenumber. The powder X-ray diffraction (PXRD) data was collected using Rigaku Miniflex diffractometer in the angular range of $2\theta = 10-70^\circ$

with CuK α radiation ($\lambda = 1.5418 \text{ \AA}$; nickel filter) and the scan speed of 1° min^{-1} . The morphological studies were accompanied using field scanning electron microscopy (FESEM) (Hitachi Model 5890).

3. Results and Discussion:

The synthesized MOF-5 material was characterized by several characterization implements to recognize its structural and morphological feature which ultimately impacting its catalytic activity. The absorption spectrum of MOF-5 was recorded using distilled water as reference. The structural analysis of MOF-5 samples was carried out via UV, FTIR, XRD and SEM techniques.

The UV-Vis spectra (Fig.1) of MOF-5 displays maximum absorption at 300nm agrees to the $\pi-\pi^*$ transition demonstrated by the π electrons of 1, 4-benzene dicarboxylic acid i.e. BDC ligand in MOF-5 and corresponds to $1A_{1g}$ to $1B_{2u}$ excitation.

FTIR investigation (Fig.2) shows the FTIR spectrum of the synthesized MOF-5. The peak at 3450cm^{-1} belongs to O-H group. The peak located in 1350cm^{-1} relates to the symmetrical vibration of the carboxyl group and the other peak observed in 1600cm^{-1} are allocated to the asymmetric vibrations of the -COOH group which is one of the chief groups of terephthalic acid ligand. The peaks in $640, 850$ and 1010cm^{-1} can be assigned to the bending vibration of the C-H bond. The peak centered at 530cm^{-1} is assigned to the Zn-O vibration in the Zn_4O group. Fourier transform infrared (FTIR) spectrum of MOF-5 displays strong bands at 1659 and 1600cm^{-1} , which match to the C=O and C-O group stretching vibration of the aromatic ring of terephthalic acid.

The PXRD pattern of MOF-5 shows (Fig.3) a peak at $2\theta = 9.8^\circ$ which corresponds to the MOF-5 crystal plane. A peak at $6.1, 9.8, 13.1, 15.6^\circ$ belongs to (200), (220), (400), (420) planes as mentioned in the literature¹⁷⁻²⁰. As shown in Fig.3, the key diffraction peaks at 6.1° and 9.8° approve the successful creation of MOF-5 crystalline phase. The intensity ratio of the powder XRD peak at 9.8° to the peak at 6.1° (denoted to as the R1 value) can be castoff to guess the adsorption possessions of a MOF-5 like materials. From the PXRD pattern of the material it is clear that the R1 value of the material is low which is responsible for the dye photodegradation properties of the synthesized MOF-5. Moreover the small R1 value, the intensity of the peak at 13.1° is high, which relates to the reflections of (400) planes of the cubic structure of MOF-5.²¹ By using Debye Scherrer equation ($D = k \lambda / \beta \cos\theta$) the particle

size was of MOF-5 material was calculated. The average crystallite size of MOF-5 was found to be 60-140nm.²²

FESEM images of MOF-5 have been represented in Fig.4. It is observed that the MOF-5 is generated of a large number of elliptical petals like structures as shown. The petals like constructions witnessed in the synthesized MOF-5 are found to be organized in regular assemblies which is distinctive in these 2D structures and in line with the previous reports¹³⁻¹⁶.

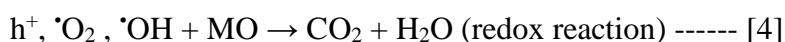
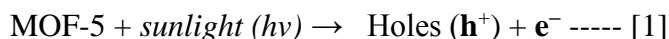
3.1 Photocatalytic activity of Methyl Orange (MO)

The dye manufacturing alone is majorly accountable for widespread ecological destruction. As a consequence, it is vital to improve novel approaches to eradicate these pollutants from water bodies entirely. Amongst numerous methods established, photo catalytic degradation has received distinct devotion due to its small cost, modest process, abolition of secondary pollutants, and operative elimination of contaminants. Keeping these things in mind the prepared sample of MOF-5 was tested for the dye photo degradation study. The methyl orange dye degradation was carried out as explained in procedure. The results obtained after 1, 4, 6 and 10 days are displayed in photographs. MO is a common organic dye, and it is very interesting to decompose it from wastewater. The photocatalytic activity of the MOF-5 is examined by revealing the MO solution comprising photocatalyst to natural sunlight radiation. There is a decrease in the peak intensities of absorption spectra (Fig.5) demonstrating the decomposition of the organic pollutant. The graph of concentration versus absorbance and time versus absorbance were plotted as shown in Fig.5 and 6 for both i.e. for reference and MOF-5. The synthesized material (MOF-5), due to its high photocatalytic activity can be efficiently cast-off for degradation of MO dye.¹⁷ It was observed that for complete MO dye degradation in presence of MOF-5 and natural sunlight, it required three to five days for various concentrations (0.05-01M) of the MO samples. Furthermore, when MO solutions of various concentrations were exposed to sunlight in absence of MOF-5, it was observed that about seven to ten days were required for complete dye degradation. It was also observed that when the amount of photocatalyst was increased from 10 to 50 mg, the photocatalytic activity was found to be increasing, which could be caused by an increased number of active sites on the catalyst surface. Further increase in the catalyst amount above 50 mg diminished the activity, which could be due to the phenomenon of light scattering. Specifically, this can be attributed to the increased collection of particles acting as obstacles

for the light irradiation¹⁷⁻²⁰. The optimum activity of synthesized MOF-5 was observed when 50mg of the material was taken in various concentrations of MO in presence of sunlight. In absence of sunlight, no dye degradation activity of MOF sample was observed.

3.2 Mechanism of photo catalysis under sunlight using MOF

The photo dye degradation includes a practice in which the catalyst absorbs energy in the form of sunlight to produce extremely reactive free radicals in a sequences of red-ox reactions. If a material is exposed to sunlight, it absorb radiations and causes electronic excitation, generating an electron-pair hole in its conduction band and valence band. These sunlight created holes can oxidize H₂O molecules adsorbed on the surface of catalyst to produce (OH[•]) radicals. Then, these ROS i.e. Reactive Oxygen Species may oxidize the dye molecules into smaller species which are harmless. MOF-based constituents display analogous properties as semiconductor photo catalysts. The valence band corresponds to the HOMO of the MOF, whereas the conduction band corresponds to the LUMO. Beneath light radiations, electrons are promoted from the HOMO of the ligand (BDC) and transitioned into the LUMO of the metal (Zn) as shown in Fig 7. The complete mechanism may be assumed from the following sequence of Red-ox reactions²².



4. Conclusion

In summary, we have synthesized the MOF-5 material using DMF as the solvent and fully characterized. The MOF-5 was designed by the facile, ecofriendly hydrothermal method and exploited as a photocatalyst. The successful preparation of MOF-5 nano-petals was confirmed through the numerous advanced analytical methods such as UV, FTIR, PXRD, and FE-SEM analysis. The photocatalytic properties of MOF-5 were confirmed by dye degradation study of methyl orange in natural sunlight. From the results obtained we can confirm that synthesized MOF-5 material has good porosity and hence can be successfully exploited for the MO degradation in presence of sunlight in small amount. It took about three to five days for complete MO dye degradation having concentrations 0.05M, 0.1M and 0.5M when exposed to 50mg of MOF-5 sample in presence of sunlight.

Figures:

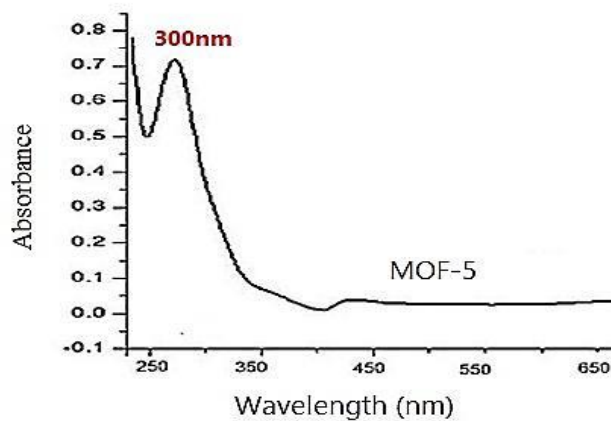


Fig.1 UV-Vis spectra of MOF-5

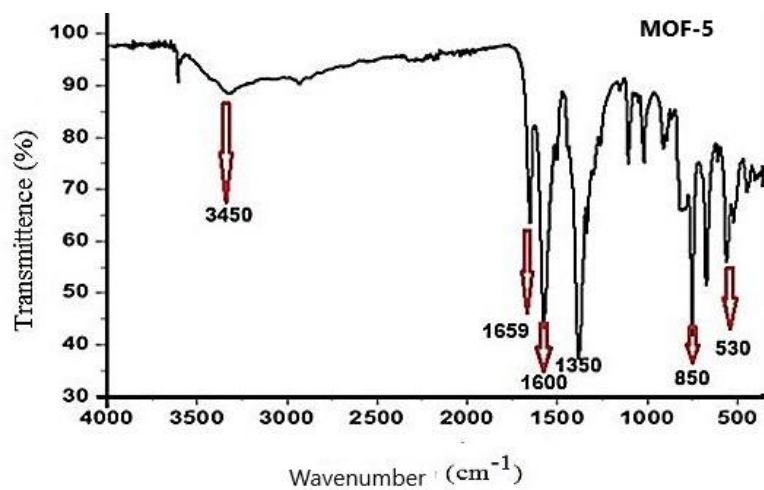


Fig.2 FTIR spectra of MOF-5

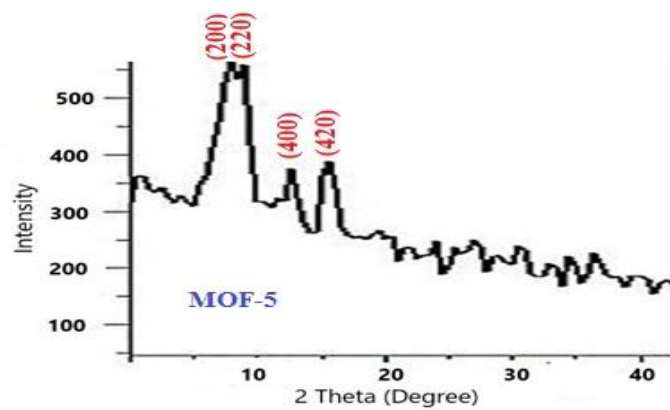


Fig.3 XRD spectra of MOF-5

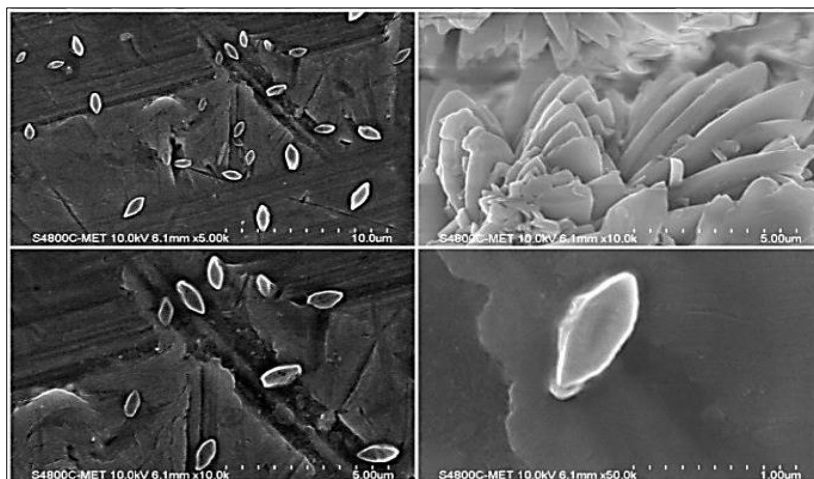


Fig.4 FESEM images of MOF-5

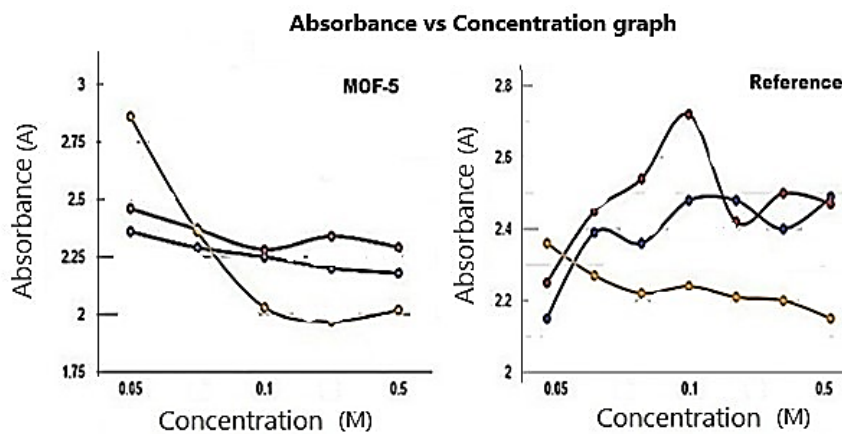


Fig.5 Absorption versus Concentration graph

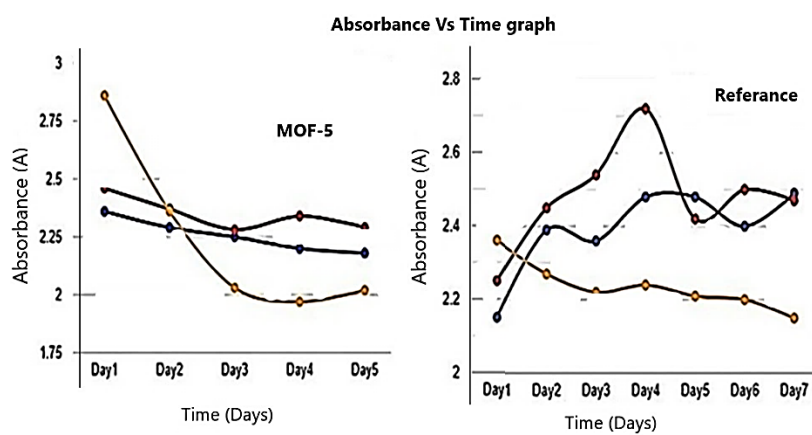


Fig.6 Absorbance versus Time graph



MO dye degradation study

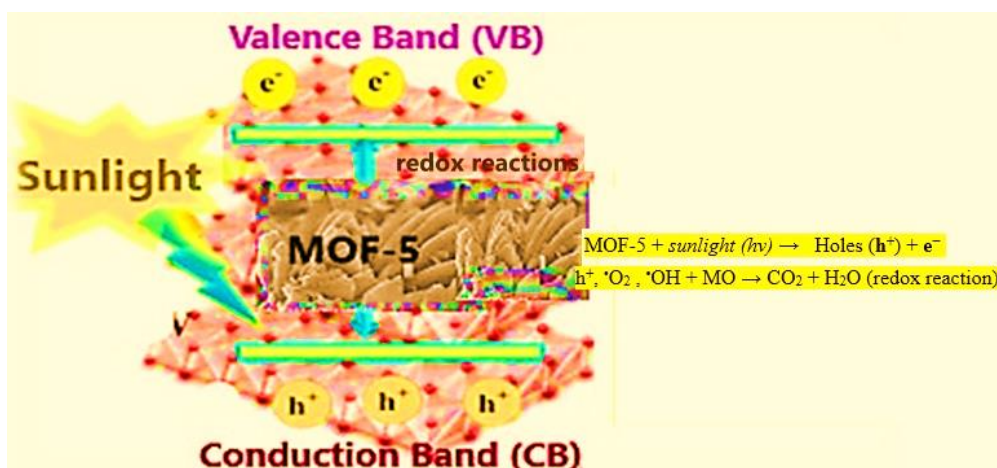


Fig.7 Mechanism of photocatalysis of MOF-5 under sunlight

References:

1. A. Chakrabortya and H. Achary, New J. Chem., 47, 1498, 2023.
2. B. Tabasum, P. Dhagale, K. Nitnaware, H. Nikule, T. Nikam, J. Environ. Chem. Eng.,7(3), 103114, 2019.
3. M. Suleman, M. Zafar, A. Ahmed, M. Rashid, S. Hussain, A. Razzaq, N. Mohidem, T. Fazal, B. Haider, Y. Park, Sustainability, 13(12), 6926, 2021.
4. S. Singh, S. Perween, A. Ranjan, J. Environ. Chem. Eng.,9 (3), 105149, 2021.
5. H. Zhao, H. Song, L. Chou, Inorg. Chem. Commun., 15, 261, 2012.
6. T. Zhang, W. Li, Q. Guo, Y. Wang, C. Li, Coatings, 12, 559, 2022.
7. X. Chen, Y. Zhang, X. Kong, K. Yao, L. Liu, J. Zhang, Z. Guo, W. Xu, Z. Fang, ACS Omega, 6, 2882, 2021.

8. A. Anum, M.A. Nazir, S.M. Ibrahim, S.S.A. Shah, A.A. Tahir, M. Malik, M. A. Wattoo, A. Rehman, *Catalysts* 13, 9849, 2023.
9. C. C. Wang, X. H. Yi, P. Wang, *Appl. Catal. B Environ.* 247, 24, 2019.
10. P. Koochi, A. Rahbar-kelishami, H. Shayesteh, *Environ. Technol. Innov.*, 23, 101559, 2021.
11. R. Ahmad, Z. Ahmad, A. Ullah, N. Riaz, M. Aslam, *Environ. Chem. Eng.*, 4, 4143, 2016.
12. M. J. Valero-Romero, G. J. Santaclara., L. Oar-Arteta, L. van Koppen, D. Y. Osadchii, J. Gascon, F. Kapteijn, *Chem. Eng. J.*, 360, 75, 2019.
13. O. Abuzalat, D. Wong, M. Elsayed, S. Park, S. Kim, *Sonochem*, 45,180, 2018
14. G. Lu, F. Chu, X. Huang, Y. Li, K. Liang, G. Wang, *Chem. Rev.*, 450, 214240, 2022.
15. M. Reza, M. Negar, M. Ashouri, *Iran. J. Sci. Technol. Trans. A Sci.*, 43, 443, 2019.
16. H. Asadevi, P. P. Nair, C. P. Amma, S. A. Khadar, S. C. Sasi, R. Raghunandan, *ACS Omega* 7, 13031, 2022.
17. Z. Z. Vasiljevic, M. P. Dojcinovic, J. D. Vujancevic, I. Jankovic-Castvan , N. B. Tadic, S. Stojadinovic, G. O. Brankovic, M. V. Nikolic, *R. Soc. Open Sci.* 7, 200708, 2025.
18. Q.V. Thi, M.S. Tamboli, Q. Thanh Hoai Ta, G.B. Kolekar, D. Sohn, *Mater. Sci. Eng. B.* 261, 114678, 2020.
19. K. Bhuvaneswari, G. Palanisamy, T. Pazhanivel, T. Maiyalagan, P. Shanmugam, A. N. Grace, *Chemosphere* 270, 128616, 2021.
20. A. Bhuyan, Md. Ahmaruzzaman, *Next Sustainability* 3, 100016, 2024.
21. B. Chen, X. Wang, Q. Zhang, X. Xi, J. Cai, H. Qi, M. Fang, 20(18), 3758, 2010.
22. H. Gupta, I. Saini, V. Singh, T. Kumar, V. Singh, *Bull. Chem. Reaction Engg. Catal.*, 19 (1),1, 2024.

Identification and Quantification of Amino Acids in Medicinal Plant Samples from Western Ghats, Maharashtra using HPTLC Technique

Vivek Rathod

Department of chemistry, S.P. Pune University, Pune 411007

Email: rathod.vivek@live.com

Received: 6.1.2025, Revised: 26.1.2025, Accepted: 27.1.2025

Abstract

This study focuses on the identification and quantification of 10 different amino acids in seven medicinal plants from the Western Ghats of Maharashtra, utilizing the High-Performance Thin Layer Chromatographic (HPTLC) technique. Notably, methionine was absent in all plant samples analyzed. Among the studied plants, *Glochidion ellipticum* demonstrated significantly high concentrations of lysine, threonine, valine, and leucine compared to other species. In contrast, *Bombax malabaricum* was found to have the lowest amino acid content.

Key words: Amino Acid Profiling, Medicinal Plants, HPTLC Analysis

1. Introduction

Since ancient times, medicinal plants have been instrumental in treating a wide range of ailments¹. In recent years, herbal medicines have gained considerable attention as alternative therapies for preventing and managing various disorders, despite the largely unknown mechanisms underlying their efficacy. This growing interest has driven extensive research aimed at analyzing medicinal plants and uncovering their potential health benefits. This growing interest has driven extensive research aimed at analyzing medicinal plants and uncovering their potential health benefits². The therapeutic properties of these plants are primarily attributed to their diverse chemical constituents, which exert significant physiological effects on the human body. Among these, bioactive compounds such as alkaloids, tannins, saponins, steroids, flavonoids, amino acids, and terpenoids are recognized for their potent antioxidant activities³.

Amino acids are crucial in protein synthesis and serve as precursors for secondary metabolites. They also engage in numerous physiological processes, including skeletal muscle function, atrophic conditions, sarcopenia, cancer, cell signalling, homeostasis, gene expression, hormone

synthesis, and protein phosphorylation, and possess antioxidant properties⁴⁻⁷ Therapeutically, amino acids are employed in treating brain metabolism and neurotransmission imbalances, enhancing immune function, and supporting cardiovascular and gastrointestinal health⁸ They are also used in managing liver diseases, fatigue, skeletal muscle damage, cancer prevention, burns, trauma, sepsis, maple syrup urine disease, and diabetes⁹. A survey of the literature reveals that there is limited data on the identification and quantification of amino acids in medicinal plants¹⁰⁻¹², hence the present work is undertaken to identify and quantify amino acids in a few medicinal plants from western ghats, Maharashtra.

Various analytical methods have been developed for amino acid determination. Early methods by Moore and Stein¹³ involved derivatization and detection in the visible region using an amino acid analyzer, which, while reliable, are costly and time-consuming¹⁴. Chromatographic techniques such as GC-MS¹⁵ RP-HPLC¹⁶ HPLC¹⁷, and capillary electrophoresis¹⁸ are also employed but are similarly time-intensive. In comparison, High-Performance Thin-Layer Chromatography (HPTLC) offers simplicity; it allows for the analysis of multiple samples at a relatively low cost and does not necessitate extensive clean-up procedures of crude samples, even for quantitative analysis. HPTLC enables the examination of the same sample at different wavelengths, providing a comprehensive profile of the plant sample^{19,20}. Consequently, HPTLC is globally utilized for characterizing crude plant drugs, pharmacologically active components, and other formulations²¹.

2. Experimental

2.1 Selection of plants

The selected plants were collected from Mahabaleswar and Bhimashankar region of Western Ghats from Maharashtra and were authenticated at Agharkar Research Institute (ARI, MACS), Pune.

The study deals with the analysis of *Glochidion ellipticum* (**bhoma**), *Aspidium cicutarium* (**Kombad nakhi**), *Mimosa pudica* (**lazalu bee**), *Bergenia legulata* (**pashan bhed**), *Mesua ferrea* Linn (**Nag keshar**), *Curculigo orchiodies* (**Kali Musli**) and *Bombax malabaricum* (**shalmali kanta**). The parts selected from these plants were leaves, rhizome, seeds, stem, anther, stem and thorns respectively.

The names of medicinal plants along with their use in medicinal plants in different treatments are mentioned below:

Bhoma-cancer, Kombad nakhi-toncils and bleeding, Lazalu-astigent, Pashan bhed-renal sone and diuretic, Nagkeshar-bleeding and inflammation, kali musali- tonic, shalmali kanta-anticoagulant and inflammation.

2.2 Preparation of plant extract

5 g of air dried plant sample was placed in the extractor of the Soxhlet apparatus and extracted with ethanol by continuous extraction for 8h, the obtained solution was concentrated on rota vapour. It was then mixed with methanol and used for HPTLC analysis

2.3 Determination of Amino acids by HPTLC technique

Each amino acid standard was prepared at a concentration of 0.5 mg mL^{-1} in methanol and water (50:50). Ninhydrin reagent was prepared by dissolving 0.6g of ninhydrin in 15 mL of glacial acetic acid and diluting it with 285 mL of iso-propanol. This reagent was used for post derivatisation of amino acids.

2.3.1 Instrument and conditions

A Camag HPTLC system with an automatic TLC sampler (Camag Linomat 5), TLC scanner 3, with UV cabinet and twin trough was used for the analysis. TLC plates of Merck, India were used for analysis with specification of 20 x 10 cm long, pre-coated with silica gel 60 F254, thickness of 0.2 mm. 100 μL syringe was used for sample spotting. The automated sampler Camag Linomat 5 was set to apply the sample spots (bands) of 8 mm length at an interval of 4 mm between the two bands and at a height of 7 mm from the bottom of the plate. Camag glass twin trough chamber was used for plate development. The developed plate was scanned using Camag TLC scanner 3 with Win CAST 1.4.4.6337 software.

2.3.2 Plate development and derivatization

The standard solutions of amino acids were prepared in methanol and water (50 :50). 15 μL of plant sample and 2 μL of standard amino acid were applied on the HPTLC plate using the Linomat-5 semi autosampler and sampling syringe. HPTLC twin trough chamber (20 X 10 cm) was pre-saturated with 15 mL of mobile phase for 10 min. The samples and standard mixtures

on the plate were run simultaneously over a migration distance of 7.5 cm. The mobile phase 1-butanol: glacial acetic acid: water (4: 1: 1) was chosen after several preliminary experiments. After development, the plate was dried in the oven at 85 °C for 5 min. the plate was sprayed with ninhydrin reagent and again dried in the oven for 5 min. the coloured spots on the HPTLC plates were then scanned with CAMAG TLC scanner linked to Win CAST software.

3. Results and Discussion

Ten different amino acids in 7 different plants were estimated in the present work. Their role human body is presented in Table 1

3.1 Analysis of plants for amino acid content

The mobile phase used for analysis of amino acids was selected on basis of prior literature reports of similar separation system and trials. To achieve effective separation of amino acids, various combination of mobile phase like 4:3:1, 4:3:3, 4:1:1 and 4:2:2 (1-butanol: glacial acetic acid: water) were tried. It was found, that 4:1:1 mixture of 1-butanol: glacial acetic acid: water gave good separation, with symmetrical and reproducible peaks of standard amino acids. The HPTLC plates were visualized at 366 and 512 nm wavelengths as shown in the Fig.1 and Fig. 2 respectively. The R_f values of the standards and colour of zone are given in Table 2

The HPTLC chromatogram of 10 amino acid standards and plant samples at 512 nm are shown in the Figs. 3 and 4 respectively.

The quantification of the amino acids present in the plants under study are compiled in the Table 3, the results are with an accuracy of +/- 2-4%.

An examination of Table 3 reveals that all the plant samples show absence of Methionine whereas, Aspartic acid (2.1 mg/g) and Proline (1.36 mg/g) were found in *Aspidium cicutarium* only. *Glochidion ellipticum* was found to be rich in Lysine (4.9 mg/g) among all the plant samples studied. *Mimosa pudica* was the only plant under study which showed presence of Histidine (0.05 mg/g). The highest amount of Threonine was found in *Aspidium cicutarium* (1.18 mg/g) whereas, it is absent in *Mesua ferrea* and *Curculigo orchiodies*. *Glochidion ellipticum* (0.85 mg/g) showed the highest Valine content whereas *Mesus ferrea* (0.12 mg/g) showed the least content.

The highest concentration of Leucine was observed in *Glochidion ellipticum* (1.55 mg/g) and was found to be absent in *Mimosa pudica* and *Bombax malabaricum*. Serine was

found only in *Curculigo orchiodies* (0.41 mg/g) and *Mimosa pudica* (0.13 mg/g). *Bergenia legualata*, *Mesua ferrea* and *Curculigo orchiodies* showed the significantly high concentration of Alanine. *Meusa ferrea* (9.46 mg/g) showed the highest Alanine content. From the Table 2 it can be summarized that *Glochidion ellipticum* is found to be rich in Lysine, Threonine, Valine and Leucine with significantly high concentrations as compared to other plants studied whereas, *Bombax malabaricum* contains lowest concentration of amino acids Leucine and Threonine.

Conclusion:

HPTLC studies of different medicinal plants from Western Ghats of Maharashtra for various amino acids estimation revealed that *Glochidion ellipticum* was found to be rich in Lysine, Threonine, Valine and Leucine with significantly high concentration as compared to other plants. Methionine was found to be absent in all the plants while *Bombax malabaricum* was found to contain the lowest amount of amino acids

Acknowledgement:

Author is thankful to UGC for meritorious fellowship and to Dr. Nilima Rajurkar, Former Professor and Head, Chemistry Department, SPPU for her constant guidance and support during this work

Figures:

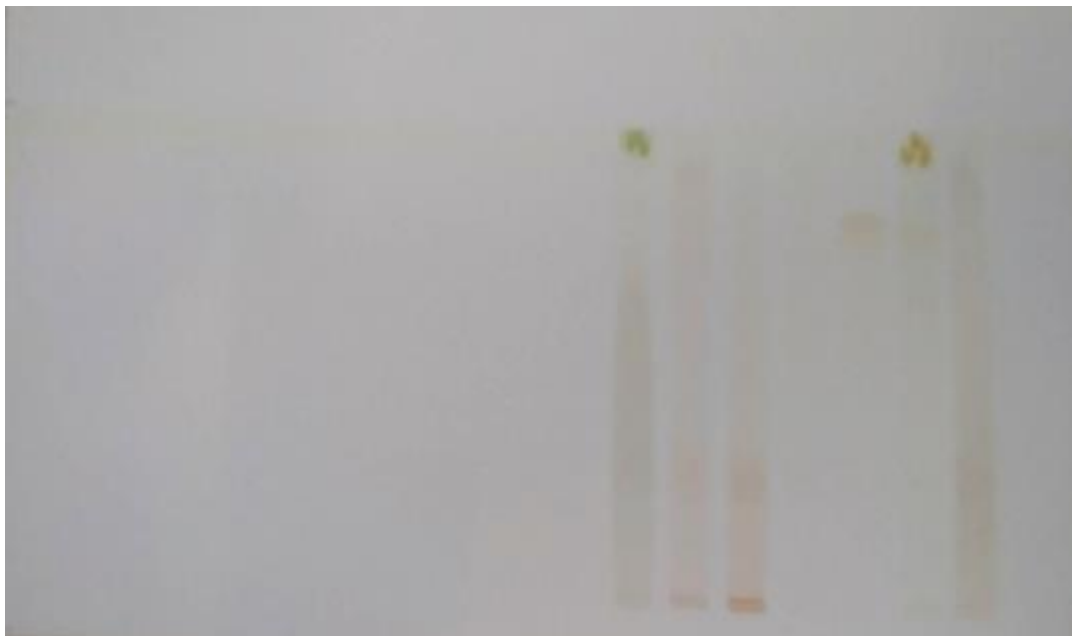


Fig.1 HPTLC plate with standards and plant samples before derivatization and visualized at 366 nm

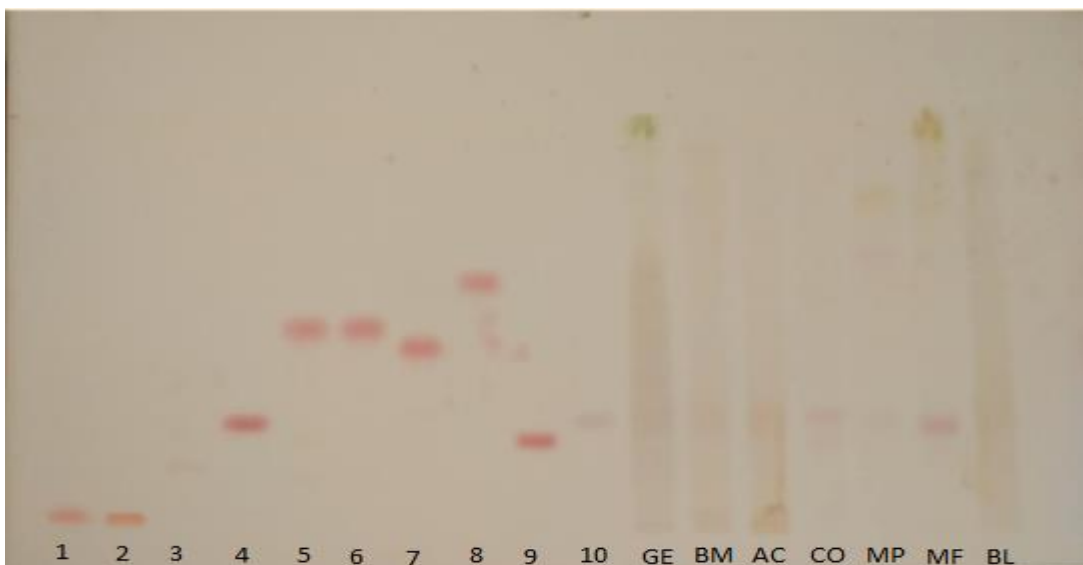


Fig. 2 HPTLC Plate with standards and plant sample after derivatization with ninhydrin and visualized at 366 nm

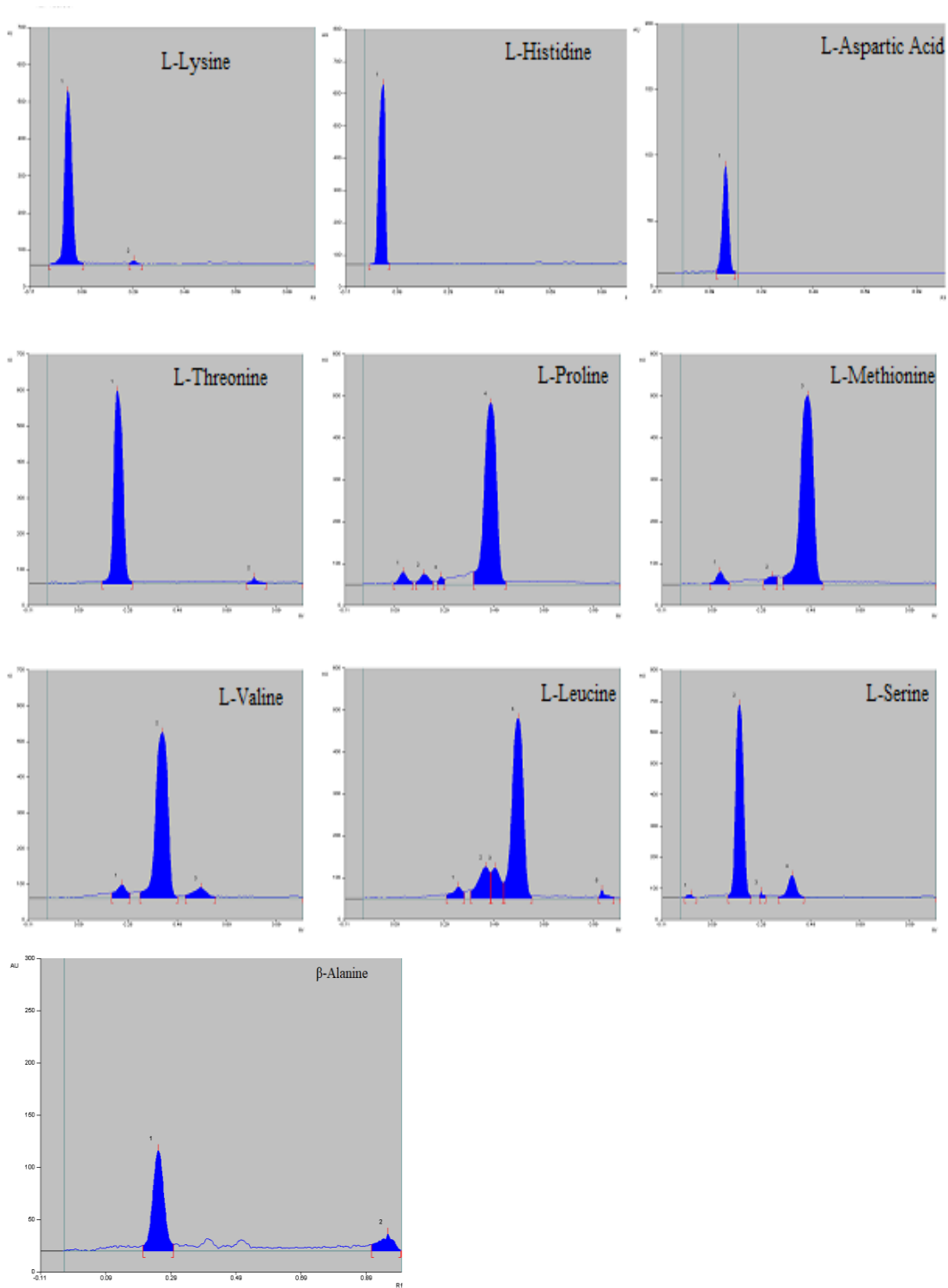


Fig.3 HPTLC chromatogram of standard Amino Acids

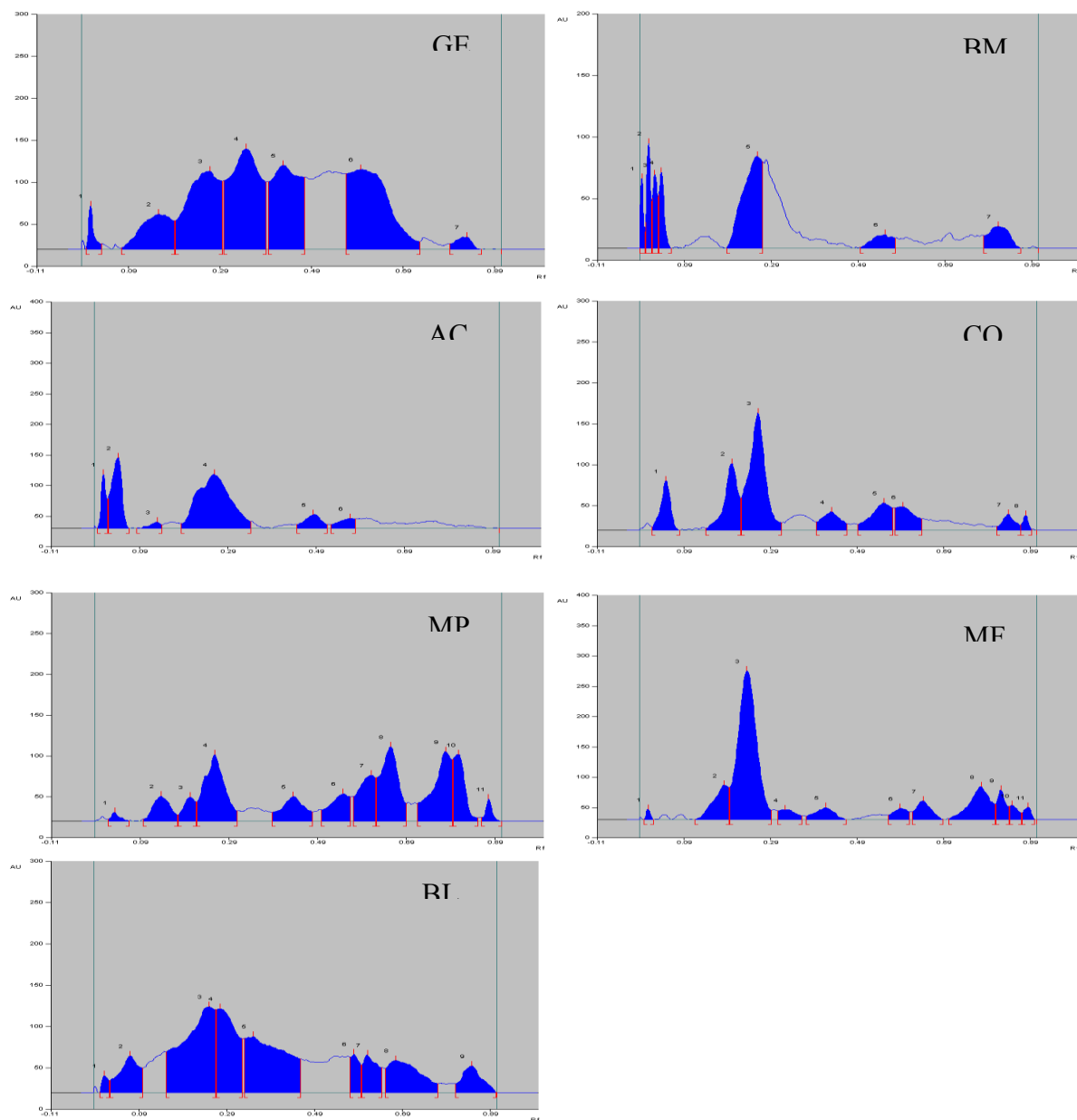


Fig. 4 HPTLC chromatogram of *Glochidion ellipticum* (GE), *Bombax malabaricum* (BM), *Aspidium cicutarium* (AC), *Curculigo orchoides* (CO), *Mimosa pudica* (MP), *Mesua ferrea* (MF), *Bergenia legulata* (BL)

Tables:

Table 1: Role of Amino Acids in human body

Sr. No	Amino acid	Role in human body
1	Alanine	Helps in metabolism of sugar and organic acids, enhances immunity and gives energy to the brain and central nervous system.
2	Aspartic acid	Helps in proper functioning of RNA and DNA, associated synthesis of immunoglobulin and antibody.
3	Histidine	It regulates the uptake of metals like Fe, Cu, Mo, Zn and Mn. It also helps in formation of metal containing enzymes.
4	Leucine	It helps in regulating blood sugar levels, stimulates growth of bone tissues and muscles and formation of growth hormones.
5	Lysine	Responsible for Ca uptake, help in building muscle protein and formation of collagen.
6	Methionine	Helps in single carbon transfer and detoxification of liver
7	Proline	Helps in maintaining strength of heart muscle, proper functioning of joints and tendons
8	Serine	Important functioning of brain, CNS and maintaining overall physical and mental health of body
9	Theronine	Supports in smooth functioning of digestive system and liver metabolism. It is part of elastin, collagen, and enamel protein.
10	Valine	Responsible for smooth functioning of nervous system, muscles, immune system and cognitive

Table 2: Rf values of standard amino acids and colour of zone detected with Ninhydrin reagent

Amino Acid	Rf value	Colour
L- Lysine	0.04	Yellow
L- Histidine	0.03	Brown
L-Aspartic Acid	0.15	Pale Violet
L-Threonine	0.26	Brown
L- proline	0.48	Brown
L-Methionine	0.45	Brown
L-Valine	0.43	Brown

L-Leucine	0.59	Brown
L-Serine	0.20	Brown
β -Alanine	0.25	Violet

Table 3: Concentration of amino acids in plant samples under study

Amino Acids Concentration (mg/g)										
Plant Name	Lysine	Histidine	Aspartic acid	Threonine	Proline	Methionine	Valine	Leucine	Serine	Alanine
<i>Glochidion ellipticum</i>	4.90	ND	ND	1.17	ND	ND	0.85	1.55	ND	ND
<i>Aspidium cicutarium</i>	1.23	ND	2.1	1.18	1.36	ND	ND	0.11	ND	ND
<i>Mimosa pudica</i>	ND	0.05	ND	0.65	ND	ND	0.21	ND	0.13	ND
<i>Bergenia legulata</i>	ND	ND	ND	0.81	ND	ND	ND	0.17	ND	ND
<i>Mesua ferrea</i>	ND	ND	ND	ND	ND	ND	0.12	0.11	ND	9.46
<i>Curculigo orchidies</i>	0.62	ND	ND	ND	ND	ND	0.13	0.23	0.41	4.77
<i>Bombax malabaricum</i>	0.32	ND	ND	0.58	ND	ND	ND	ND	ND	ND

ND = Not Detected

References:

1. C. K.Kokate, S. B. Purohit and S.B. Gokhale Pharmacognosy, Chapter 14. 43rd Edition. Nirali Prakashan Publication, Pune, 2009.
2. S.Palani, S. Raja, D. Venkadesan, S. Karthi, K. Sakthivel and B.S. Kumar., Archives Appl. Sci. Res., 1(1), 18, 2009.
3. Y. Cai, L. Qiong, S. Mei and C.Harold, Life Sci. 74, 2157, 2004.
4. E.F.Moran-Palacio, O.Tortoledo-Ortiz, G.A.Yañez-Farias, L.A. Zamora-Álvarez, N.A.Stephens-Camacho, J.G.Soñanez-Organis, L.M.Ochoa-López, J.A. Rosas-Rodríguez, Trop. J. Phram. Res. 13 (4), 601, 2014.
5. S.K. Bardaweel, J. Med. and Bioengineering. 3 (3), 195, 2014.
6. W. Vollmer, D. Blanot. and M.A. de Pedro, FEMS Microbiol. Reviews. 32, 149, 2008

7. G.Wu, *Amino Acids*, 37(1), 1, 2009.
8. C.D. Meletis and J.E. Barker, *Alternat. and Complement. Therapies*. 11, 24, 2005.
9. N. Tamanna and N. Mahmood, *Inter. Scholarly Res. Notices*. 2014, 1, 2014.
10. J. O. Odukoya, J. O. Odukoya, E. M. Mmutlane and D. T. Ndinteh *Pharmaceutics* 13(9), 1367, 2021.
11. L. Budniak, L. Slobodianiuk, S. Marchyshyn and I. Potishnyi *Pharmacia* 69(2), 437 2022.
12. P. Wang, L. Xiao, S. Zheng, J.Pang and J. Chen, *Ind. Crops Products* 212, 118306, 2024.
13. S. Moore and W. H. Stein, Academic Press, New York, 6, 819, 1963.
14. G. Sarwar and H. G. Botting, *J. Chromatogr.* 615 (1), 1, 1993.
15. B. Emanuele, F. C. Maria, G. S. Anna G., M. Gian Luigi and L.Giovanni, *Apidologie*. 34, 129, 2003
16. K .L. Woo, Determination of Amino Acids in foods by reversed- phase high performance Liquid chromatography. In: Copper C., Packer N., *Amino Acid analysis protocols*. Human Press, Totowa, NJ, Williams, 2001, 141
17. J. Igor, S. Krstović, D. Glamović, S. Jakšić and B. Abramović , *J. Serb. Chem. Soc.* 78 (6), 839, 2013.
18. M. Ummadi and B. C.Weimer, *J. Chrom. A.* 964 (1-2), 243, 2002.
19. S. Wagner, A. Ureña, E. Reich and I. Merfor, *J. Pharm. Biomed. Anal.* 48, 587, 2008.
20. K. Dhalwa, V.M. Shinde, Y.S. Biradar and K. R. Mahdik, *J. Food Compos. Anal.* 21, 496, 2008.
21. I. Khan, P. L. Sangwan, J.K. Dhar and S. Kul, *J. Sep. Sci.* 35, 392, 2012.

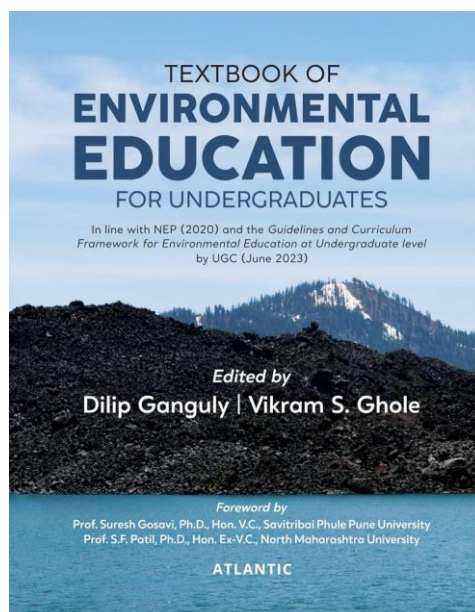
Book Review: Textbook of Environmental Education for undergraduates- Edited by Dilip Ganguly and Vikram S. Ghole

Dr. Nilima Rajurkar

Former Professor and Head Chemistry Department and Former Head, Environmental Science
Department, Savitribai Phule Pune University, Pune 411007

Editor in Chief, J. ISAS

Email: rnilima@rediffmail.com



Textbook of Environmental Education for Undergraduates, edited by Dr. Dilip Ganguly and Dr. Vikram Ghole, is a significant contribution to the academic world, thoughtfully aligning with the National Education Policy (2020) and the curriculum framework for environmental education outlined by the University Commission (June 2023). This book provides a detailed exploration of critical environmental topics and serves as an excellent resource for students and educators alike.

The book begins by examining the interaction between humans and the environment, gradually delving into essential themes such as the sustainable use of natural resources, the pressing environmental issues arising from human interventions, and the need for biodiversity conservation. It addresses various types of pollution, their impacts on human health, and the growing challenge of climate change. Concluding with discussions on environmental management, treaties, and legislation, the text offers a well-rounded perspective on the subject.

The book is systematically divided into eight units, covering a wide array of vital topics:

- **Humans and Environment** – Exploring the intricate relationship between human activities and their environmental impact.
- **Resources and Development** – Delving into the sustainable use of natural resources and their role in development.
- **Environmental Issues: Local, Regional, and Global** – Addressing the spectrum of environmental challenges at various scales.
- **Conservation of Biodiversity and Ecosystems** – Highlighting the importance of preserving biodiversity and maintaining ecological balance.
- **Environmental Pollution and Health** – Discussing the effects of different types of pollution on health and the environment.
- **Climate Change: Causes, Impacts, and Mitigation Measures** – Analyzing the causes and consequences of climate change while proposing actionable solutions.
- **Environmental Management** – Offering insights into sustainable environmental practices and strategies.
- **Environmental Treaties and Legislations** – Providing an overview of significant international and national efforts to safeguard the environment.

What sets this book apart is its student-friendly approach. Each chapter includes thought-provoking questions and project ideas, fostering critical thinking and application-based learning. Additionally, links/QR codes for further reading encourage students to explore the subject in greater depth. The simple and lucid language ensures that learners from diverse academic backgrounds can easily comprehend and appreciate the content.

This book will undoubtedly benefit undergraduate students, postgraduate students, and aspirants preparing for competitive examinations. Congratulations to Dr. Dilip Ganguly, Dr. Vikram Ghole, and the team of 18 expert authors for creating this well-rounded and insightful guide to environmental education.

The book is published by Atlantic publishers & distributors and is available on www.atlanticbooks.com.